Analyzing the 3D morphology of particle systems coated by mechano-fusion using micro-CT image data

Philipp Rieder[1*], Phillip Gräfensteiner[1*], Judith M. Seyffer[2], Tom Kirstein[1], Nora Brachhold[3], Christos G. Aneziris[3], Volker Schmidt[1], Urs A. Peuker[2]

July 14, 2026

[1]Institute of Stochastics, Ulm University, D-89069 Ulm, Germany

[2]Institute of Mechanical Process Engineering and Mineral Processing, Technische Universität Bergakademie Freiberg, D-09599 Freiberg, Germany

[3]Institute of Ceramics, Refractories and Composite Materials, Technische Universität Bergakademie Freiberg, D-09599 Freiberg, Germany

*Corresponding authors. philipp.rieder@uni-ulm.de, phillip.graefensteiner@uni-ulm.de;

PR and PG contributed equally to this paper.

Abstract

Particle coating is a widely used strategy for tailoring particle properties to specific applications, with the morphology of the coating layer strongly influencing the effective properties of the resulting hetero-aggregates. Dry particle coating by means of mechano-fusion (MF) has gained increasing attention in applications such as battery material manufacturing, where coating layers surrounding host particles can significantly enhance performance and lifetime. To improve the understanding of process–structure relationships and consequently optimize the coating process, detailed characterization of the resulting hetero-aggregates is essential. In this paper, several geometric descriptors are introduced for the quantitative analysis of coating structures, including mean coating thickness, surface area coverage, and contact loss. In addition, correlations between these descriptors are investigated to provide a more comprehensive understanding of the interactions that govern the coating process. The analysis is based on micro-computed tomography (CT) images of a model particle system consisting of PTFE-coated alumina particles produced by MF. To reduce artifacts arising from the embedding of coated particles in epoxy, a hierarchical segmentation pipeline was developed for micro-CT image processing.

Keywords: Hetero-aggregate; dry particle coating; mechano-fusion; micro-CT; statistical image analysis; geometric descriptor

1 Introduction

The dry particle coating process mechano-fusion (MF), originally developed in the 1980's [1, 2], has recently been used more frequently in different applications ranging from pharmaceuticals [3, 4], matrix-reinforced composite materials [5, 6], to lithium-ion battery (LiB) materials [7, 8]. The various advantages of dry coating are particularly beneficial in the manufacturing of functionalized battery materials: (i) the coating occurs at the level of individual host particles with smaller individual guest particles, and uniform coatings (core-shell type aggregates) with predefined coating thicknesses can be synthesized, (ii) MF does not rely on the use of liquid solvents, which reduces processing efforts, costs, and environmental impacts [9], and (iii) the process is scalable and can be performed in continuous operation [10].

The type of functionalization of the host particles in the context of battery materials, *e.g.*, cathode active materials (CAM), depends on the specific particle system to be processed. Several examples of MF coating for LiB materials have the objective of increasing mechanical or chemical stability, and electronic conductivity of lithium-nickel-manganese-cobalt oxide (NMC) used as CAM [7, 11–15].

As a result, superior specific capacity, energy density, and long-term cycling stability can be achieved [14]. For the optimization of the newest generation of all-solid-state batteries (ASSB), a sufficiently close solid-solid contact must be established between CAM and solid electrolyte (SE) to allow the transfer of lithium ions [12, 16, 17], since geometric physical contact losses between two materials result in high interface resistances. In general, the performance of any battery electrode material is highly dependent on the optimization of the underlying microstructure [18–22].

Thus, MF is applied to coat CAM host particles with SE [12, 15, 16] or an artificial cathode electrolyte interface material [23] as guest particles. Compared to merely mixing CAM and SE, the coating requires less SE content because interfacial contact and total contact area are significantly improved [16]. Currently, different types of materials are employed as SE, *e.g.*, polymer-lithium salts, glass, or (glass-)ceramic type SEs [24]. From the latter, (crystalline) sulfide SE, *e.g.*, lithium thiophosphate chloride (LPSCl), shows very high ionic conductivities ($1.9{\cdot}10^{-3}\,\mathrm{S\,cm^{-1}}$) [24–26] but low intrinsic electronic conductivity ($1.6{\cdot}10^{-8}\,\mathrm{S\,cm^{-1}}$) [27, 28]. In contrast, NMC is characterized by dominating electronic conductivity ($10^{-4}\,\mathrm{S\,cm^{-1}}$ to $10^{-2}\,\mathrm{S\,cm^{-1}}$) and low ionic conductivity ($3.7{\cdot}10^{-9}\,\mathrm{S\,cm^{-1}}$ to $9.1{\cdot}10^{-9}\,\mathrm{S\,cm^{-1}}$) [29]. The difference in particle size and stiffness (CAM: larger, rigid, and brittle particles; sulfide SEs: smaller, soft, and ductile particles) facilitates the coating.

The dry coating mechanism using the hybridization of a deformable model material, sulfide SE, is described as room temperature pressure sintering [30]. Mechanical energy input leads to plastic deformation of the initially discrete individual guest particles of SE, so a continuous SE coating is obtained on the surface of the host CAM particles. The

deformation of guest particles during MF was investigated recently by atomic force microscopy [31]. Structural characterization using different 2D and 3D imaging techniques, *e.g.*, scanning electron microscopy (SEM) in combination with focused ion beam (FIB) milling and micro- or nano-computed tomography, is essential to understand the resulting microstructure of particles after coating, to be used as advanced battery materials.

In this paper, a model material system of alumina host particles and polytetrafluoroethylene (PTFE) guest particles is dry coated with MF to produce hetero-aggregates mimicking SE coated CAM particles. 3D image data of the resulting aggregates is acquired by micro-computed tomography (CT) measurements. After image processing to segment the host particle and guest phase, various geometric descriptors are computed to quantitatively characterize the morphology of the hetero-aggregates. In particular, geometric descriptors that characterize the coating, such as the mean coating thickness, the surface area coverage of host particles, and the degree of contact loss between the host and guest phase are considered. The statistical relationships between these descriptors are investigated with the aim of studying various factors influencing the quality of the coating structure, *i.e.*, the outcome of the coating by MF. Although the materials considered in this study serve merely as a model system and are not directly applicable to LiB manufacturing, the developed synthesis and analytical analysis methods are applicable to general hetero-aggregate particle systems produced by MF or related coating techniques. These methods enable quantitative characterization of particle morphology, improve the understanding of process-property relationships, and thereby facilitate the identification of critical factors affecting coating quality.

2 Materials and Methods

2.1 Particle system

The need for a controlled processing atmosphere with a very low residual air moisture content and the associated safety concerns [32] favor the use of model materials rather than sulfide SE materials. As described previously, a soft, deformable model material needs to represent the sulfide SE, accompanied by larger sized, brittle, relatively spherical host particles representing CAM. It is important to note that the chosen particle system is scaled up by a factor of approximately 5 to 9 (median particle size of commercially available NMC particles is 5 µm to 10 µm [33]). The up-scaling ensures the capability of micro-CT to fully resolve the guest particle structure. In addition, the particle system focuses on the electrode components CAM and SE only. At this point, conductive additives or binder are not considered.

PTFE particles (FP30-PD-000110, Goodfellow GmbH, Hamburg, Germany) with a density $\rho_{\text{guest}} = 2.2\,\text{g}\,\text{cm}^{-3}$ and a median particle size of 9.5 µm were acquired and served as

guest particles. SEM images of the pristine PTFE particles are shown in Figure 1(a). Due to their synthesis process, the PTFE particles show irregular shapes and form aggregates consisting of a large number of primary particles.

The host particles were chosen to be spherical alumina (DAW-45, Denka Chemicals GmbH, Düsseldorf, Germany) with a density $\rho_{\text{host}} = 3.95\,\text{g}\,\text{cm}^{-3}$ and a median (volume-weighted) particle size of 45.3 µm. The median (volume-weighted) particle sizes are derived from the particle distribution of pristine PTFE guest particles and alumina host particles. Both are measured via laser diffraction using the dry dispersing unit Aero S at 3 bar (Mastersizer 3000, Malvern Panalytical GmbH, Kassel, Germany), see Figure 2(a). The particle size distribution of alumina is rather narrow and only a small number of particles deviate from ideal sphericity, with some showing open cracks, pores, larger cavities, distinct surface roughness, smaller satellite particles, and rarely completely irregularly shaped particles. Thus, these particle geometries strongly resemble those of NMC particles. The (surface) features mentioned above are observable in the SEM images presented in Figure 1(b), where image acquisition relies on the XL 30 ESEM (FEI Europe B.V., Eindhoven, The Netherlands) at low acceleration voltages of 1...3 kV.

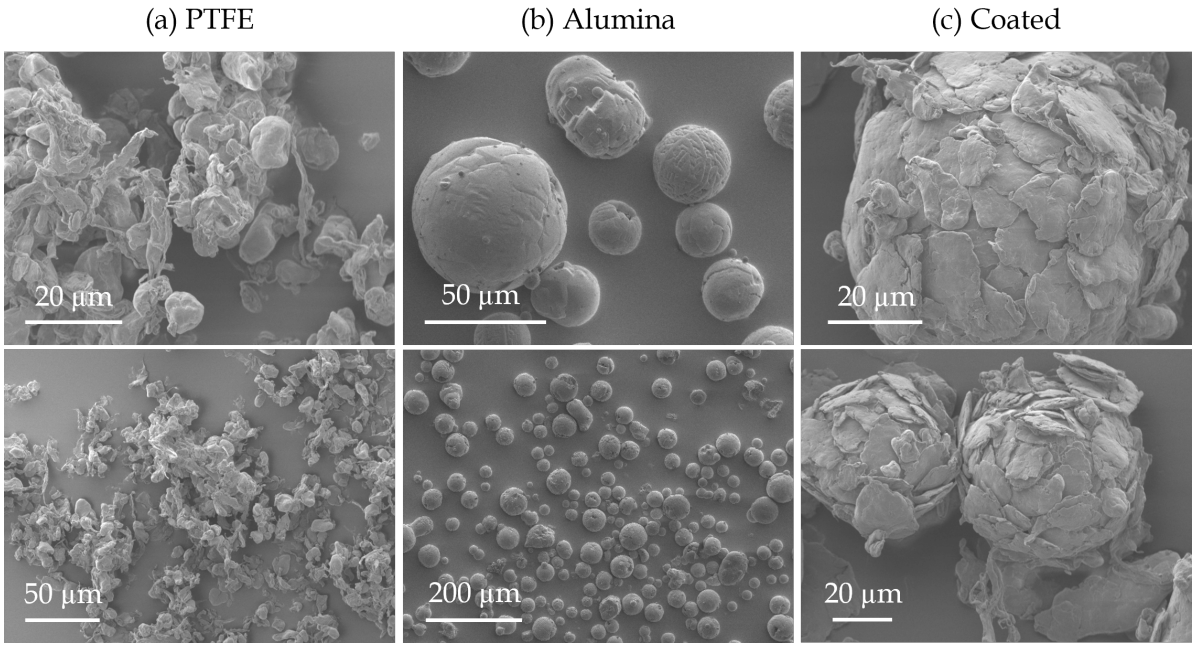

Figure 1: SEM images of different magnifications for pristine PTFE (a), pristine alumina (b) and the coated particles after MF (c).

2.2 Mechano-fusion coating

Dry particle coating of alumina with PTFE (guest phase) is performed via MF using the Angmill Mechano-Fusion (AMS) setup of the Picobond module in combination with the small-scale, multi-processing machinery platform Picoline (Hosokawa Alpine GmbH,

Augsburg, Germany). The AMS is a rotor-stator type high energy mixer where the particles to be processed are forced into a small gap between rotor and stator. A scraper removes any adhering material from the rotor. For a scheme of the process, we refer to a previous publication [34]. The guest-particle weight ratio is determined by targeting 100 % surface area coverage (SAC) of host particles with a monolayer of spherical guest particles. Assuming that all host and guest particles are each of the same sizes $d_{\mathrm{host}} = 43.3\,\mu\mathrm{m}$ and $d_{\mathrm{guest}} = 7.5\,\mu\mathrm{m}$ (based on manufacturer's specifications) with densities ρ_{host} and ρ_{guest} (see above) respectively, the corresponding weight percentage of guest particles wt%(G) is estimated by

$$\mathrm{wt\%}(G) = \frac{N d_{\mathrm{guest}}^3 \rho_{\mathrm{guest}}}{(d_{\mathrm{host}}^3 \rho_{\mathrm{host}}) + (N d_{\mathrm{guest}}^3 \rho_{\mathrm{guest}})}, \tag{1}$$

where

$$N = \frac{4(d_{\mathrm{host}} + d_{\mathrm{guest}})^2}{d_{\mathrm{guest}}^2}, \tag{2}$$

see [35]. This results in a guest-particle weight ratio of 34.7 %, which is close to those reported for SE in the literature, *e.g.*, 10 % to >30 % [9, 16, 30, 36]. This weight ratio of 34.7 % corresponds to a volume-weighted host particle fraction of 51.2 %. After a short ramp-up phase, the coating is performed at 5000 min^{-1} for 10 min. The clearance between the rotor and stator remains fixed at 2 mm, and the process chamber volume is filled up to 30 % with material. The coated particles after MF are imaged by SEM, see Figure 1(c). The experimental setup successfully produces coated particles at the given processing parameters. The surfaces of alumina host particles are coated with strongly deformed PTFE guest particles, predominantly forming a primary continuous layer with some protruding, weakly attached guest particles on the outer surface. The preparation of samples for micro-CT imaging is expected to remove any weakly attached PTFE guest particles due to the shear forces acting on the coating during the mixing with a highly viscous epoxy resin. However, from those SEM images alone, it is not possible to deduce whether the primary coating layer is completely continuous, *i.e.*, film-like, or partly discrete.

2.3 Image acquisition

2.3.1 Sample embedding and micro-CT imaging

A workflow for the non-destructive 3D characterization of micron-sized particles using micro-CT that focuses on statistical significance has been established in [37] and serves as the general approach for sample preparation and micro-CT imaging in this study. Firstly, a representative sample of MF coated particles is produced by splitting using a micro riffler (QuantaChrome Instruments, Boynton Beach, USA). Then, the sample is mixed at a ratio of 3:2 by volume with a nano-sized spacer material (Lamp black 101,

1.77 g cm^{-3}, Orion Engineered Carbons GmbH, Cologne, Germany), where the mixture is carefully blended by hand stirring into a two-component epoxy at a 1:1 weight ratio. Thereby, any PTFE guest particles that are only loosely attached are removed from the surface of the coated host particles. Upon achieving a homogeneous paste-like state, the sample is suctioned into a polymer tube and left to cure for 24 h. After curing, a cuboid of approximately 1 mm×1 mm×2 mm is cut and attached to a metal pin with glue. 3D micro-CT imaging is performed with an Xradia 510 Versa (Carl Zeiss Microscopy GmbH, Oberkochen, Germany), which, in addition to the setup of a conventional micro-CT, features an optical magnification unit. The scanning parameters are optimized for the use of the highest optical magnification (40 times) near the resolution limit of the device with a voxel size of 0.4 µm. The acceleration voltage is set to 80 kV at 7 W power, and the Zeiss standard low energy filter 2 is inserted. 1601 projections are acquired with an exposure time of 18 s each. To increase the number of observed particles, two disjoint regions, one in the lower part and the other in the upper part of the cuboid sample, are imaged. The data are reconstructed using the Zeiss Reconstructor (Carl Zeiss AG, Oberkochen, Germany) filtered back projection algorithm and standard settings. Byte scaling during reconstruction ensures the same range of gray values in the histograms of the upper and lower samples. No image post-processing is performed before segmentation. Figure 2(b) shows a representative cross-section of the reconstructed micro-CT image data, which reveals that the guest particle coating is mostly continuous but in some positions shows delamination of the coating. This contact loss between host and guest particles can be suspected, but is difficult to fully resolve at the host-guest particle interface.

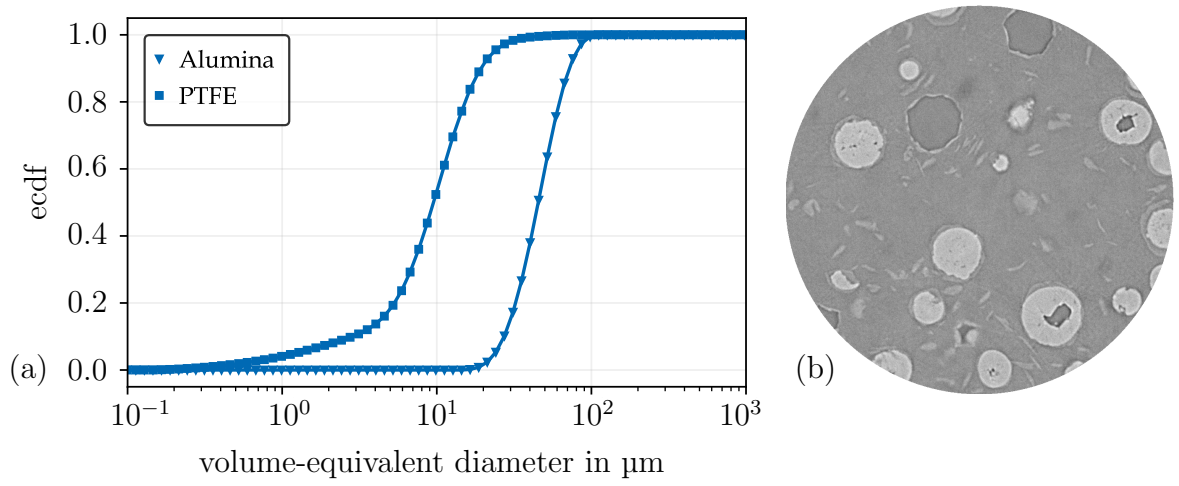

Figure 2: (a) (Volume-weighted) empirical cumulative distribution function (ecdf) of particle sizes of pristine alumina and pristine PTFE, measured with laser diffraction and dry dispersion at 3 bar, along with a 2D cross section of the reconstructed micro-CT image (b).

2.3.2 Sample polishing and high-resolution SEM imaging

After micro-CT scanning, high-resolution SEM images are acquired of several polished sections across the z-axis (height) of the original micro-CT sample. In order to polish the sample, it is re-embedded in epoxy to be mounted onto the standardized sample holder of the polishing machine (LaboForce-100, Struers ApS, Ballerup, Denmark). During polishing, the sample is pressed to the surface of a very fine silicon carbide polishing disc with a contact force of 30 N. Once the upper surface of the cuboid is reached, the sample is polished for 15 s and then prepared for SEM imaging by sputtering with carbon. The high-resolution SEM images are acquired with a Tescan Amber (Tescan, Brno, Czech Republic) at 15 keV using the back scattered electron detector and a field of view of 500 µm. The resulting image resolution is 0.12 µm. The SEM images of the polished sections are used for an additional visual inspection of the coating structure; see Figure 3.

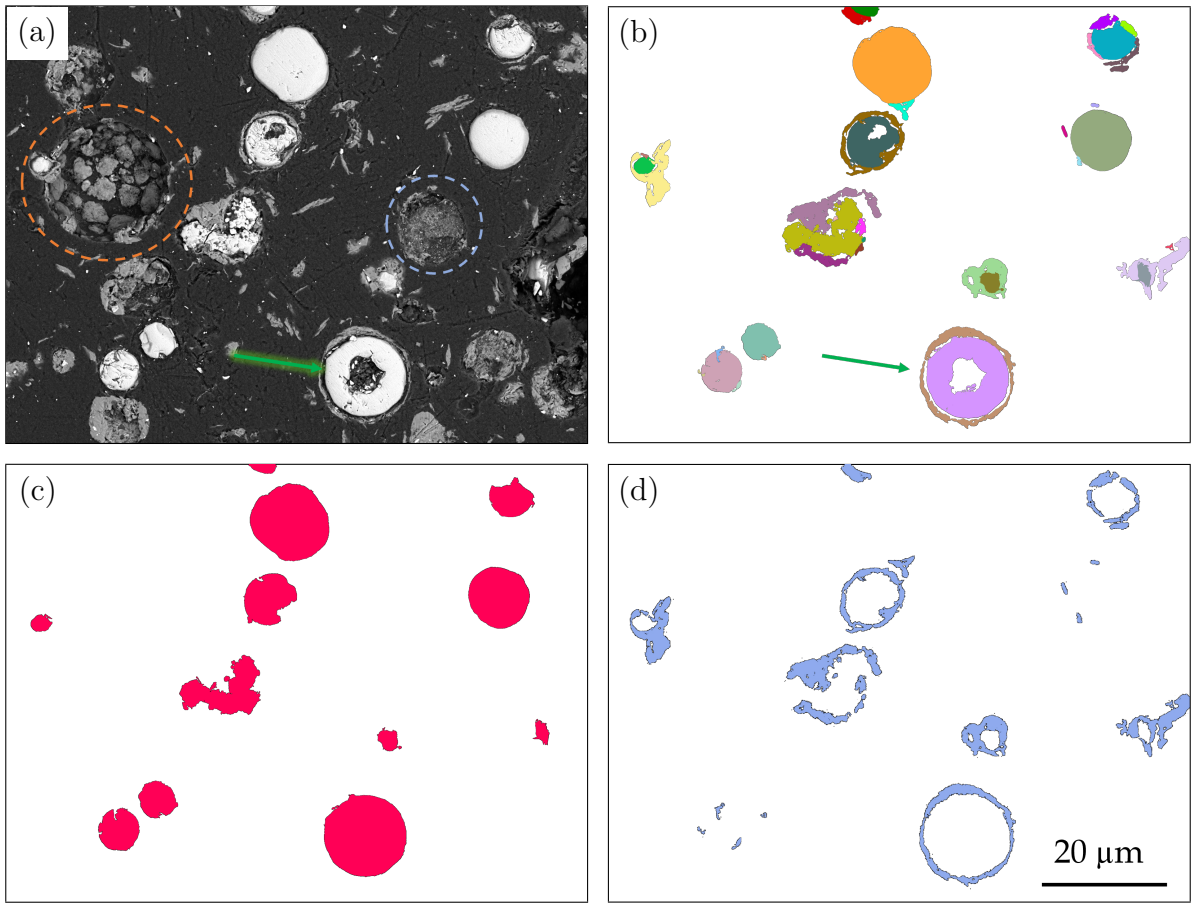

Figure 3: High resolution SEM image after polishing of the sample, green arrow: contact loss of alumina and coating, orange dashed line: air bubble, blue dashed line: removed alumina host particle due to polishing (a). Segmented regions of alumina host and attaching PTFE guest phase (b). Extracted alumina host phase (c) and PTFE guest phase (d).

The delamination of the coating layer, suspected in the micro-CT images, is confirmed by the SEM images, see the green arrow in Figure 3(a). After applying a supervised ma-

chine learning-based algorithm (based on a Random forest classifier) to derive a semantic, phase-wise segmentation of host, guest, and background material (epoxy) in ilastik [38], this effect becomes more pronounced, see Figure 3(b). So far, previous experiments with other materials (alumina host and polystyrene guest particles) [39] and SEM images of non-embedded particles (see Figure 1(c)) did not indicate the presence of a gap formed by delamination between the host and guest particle phases. However, such gaps, *i.e.* local contact losses, are of particular interest in battery technology due to their occurrence in LiBs caused by cycling induced volume changes [9, 36, 40]. The orange and blue encircled regions in Figure 3(a) indicate an air inclusion originating from the sample preparation, where PTFE particles accumulate, and a PTFE coating region lacking a host particle due to its removal during polishing, respectively. In those areas, the SEM image strongly differs from the respective micro-CT cross-sectional image due to artifacts of sample preparation.

Note that further high-resolution SEM images and the trained segmentation model (pixel and object classification using the trained machine learning in ilastik) are available in a repository, see the Data Availability statement at the end of this paper.

2.4 Image segmentation

In this section, the segmentation procedure applied to previously acquired micro-CT images is outlined. First, in Section 2.4.1 the phase-wise segmentation is described, *i.e.*, each voxel is classified as host, guest, air inclusion, or background. Subsequently, Section 2.4.2 presents the instance-wise segmentation used to identify individual aggregates. As the coating frequently exhibits guest regions arranged perpendicular to the surface of host particles, such artifacts arising from sample embedding are identified in Section 2.4.3.

2.4.1 Phase-wise segmentation

Let $I\colon W \to \{0, 1, \ldots, 255\}$ denote the grayscale image derived by micro-CT scanning as described in Section 2.3.1, where $W \subset \mathbb{Z}^3$ denotes the cylindrical sampling window, and $\mathbb{Z} = \{\ldots, -1, 0, 1, \ldots\}$ represents the set of integers. The phase-wise segmentation of I is given by the mapping $I_{\text{phase}}\colon W \to \{0, 1, 2, 3\}$, defined as

$$I_{\text{phase}}(x) = \begin{cases} 1, & \text{if } x \text{ corresponds to the host phase,} \\ 2, & \text{if } x \text{ corresponds to the guest phase,} \\ 3, & \text{if } x \text{ corresponds to the air inclusion phase,} \\ 0, & \text{else,} \end{cases} \tag{3}$$

for each voxel $x \in W$, where the guest phase is given by $\mathcal{G}^{\text{all}} = \{x \in W\colon I_{\text{phase}}(x) = 2\}$. Note that the phase-wise segmentation I_{phase} was obtained using the commercial software

Dragonfly (version 2024.1) [41]. More precisely, a 3D U-net [42] of depth 4 with an initial filter count of 32 and batch normalization was trained on hand-labeled cutouts of several slices of I first to distinguish between host, guest, and background phase. The background phase encompasses both the epoxy spacer matrix and its air inclusions, as well as the pores of the alumina host particles. Subsequently, a 2.5D U-net of depth 5 with an initial filter count of 64, which takes three slices into account, is used to identify air inclusions. Note that individual air inclusions consisting of less than 4000 voxels ($\approx$ 6.9µm^3) are considered noise and classified as background. An exemplary cross section of I_{phase} is shown in Figure 4(b).

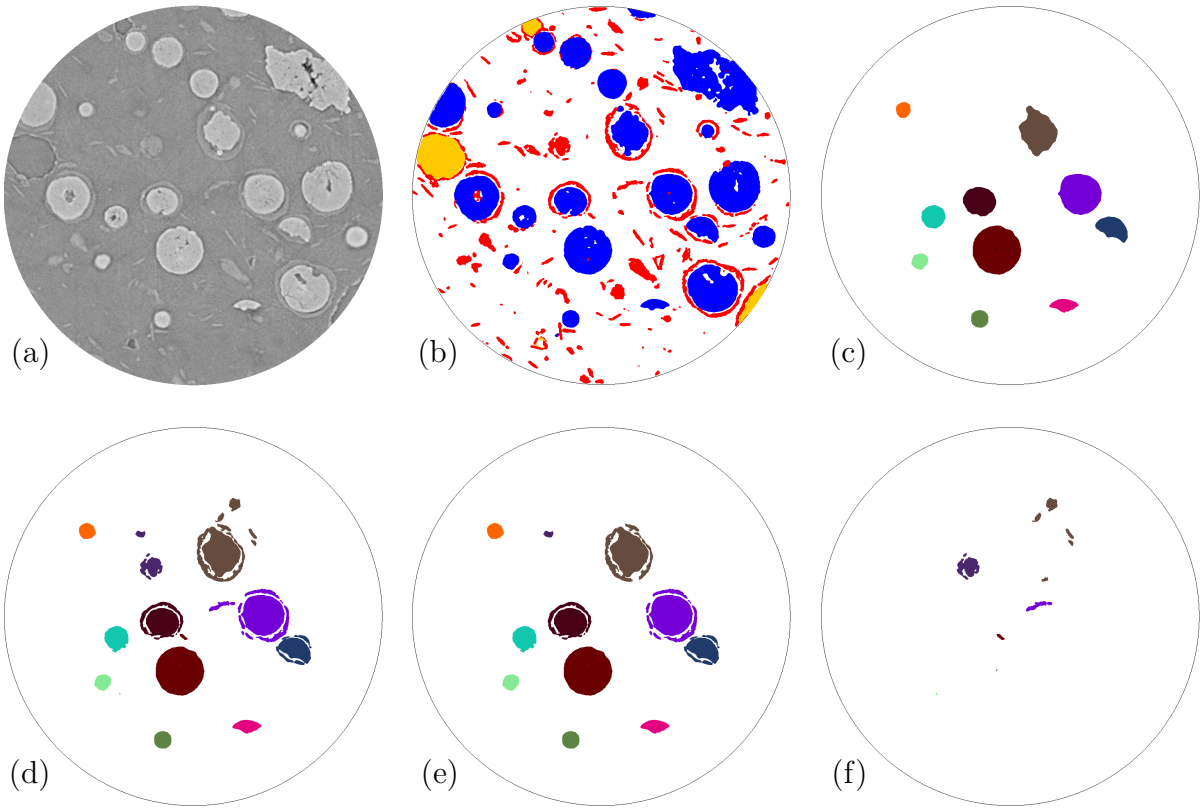

Figure 4: 2D cross sections visualizing the segmentation procedure applied to a micro-CT image: grayscale image (a), phase-wise segmentation I_{phase}, where blue, red, and yellow colors indicate host, guest, and air inclusion phases, respectively (b). False colors in the host-wise I_{host} (c) and aggregate-wise I_{agg} (d),(e) segmentations, introduced in Section 2.4.2 below, distinguish individual hosts and aggregates. In (e), the perpendicular guest region is removed, differences to (d) are highlighted in (f). Note that some aggregates may appear disconnected in 2D. Aggregates excluded in (b)–(f) are not fully contained in the sampling window, contain multiple hosts, or contact an air inclusion.

2.4.2 Aggregate-wise segmentation

In this section, the phase-wise segmentation I_{phase} introduced above is used to obtain an aggregate-wise segmentation that assigns a unique label to each aggregate, *i.e.*, all

voxels of $W \subset \mathbb{Z}^3$ belonging to the same aggregate share the same label. For this, first a host-wise segmentation is determined by detecting individual host particles. In conjunction, the host-wise segmentation is used to obtain a guest-wise segmentation, where each voxel of the guest phase is assigned the label of the host particle to which it is connected. Together, the host- and guest-wise segmentations result in the aggregate-wise segmentation used throughout the remainder of this paper.

More precisely, the host-wise segmentation $I_{\text{host}} \colon W \to \{0, 1, \ldots\}$ is obtained by applying a connected component algorithm, as implemented in *scikit-image* [43], to the host phase of the mapping I_{phase} given in Eq. (3). This algorithm algorithm results in an initial mapping $\mathrm{C}_{\text{host}} \colon W \to \{0, 1, \ldots\}$ that assigns a unique label to each connected component of the host phase, where the value 0 is reserved for all voxels not belonging to the host phase. From this initial segmentation, all connected components that comprise fewer than 100 voxels are discarded, as they are likely due to measurement noise or misclassification in the earlier image segmentation steps. Subsequently, morphological closing [44] with a sphere-shaped structuring element of radius $r = 15$ voxels is applied to the reaming region to close holes within host particles. These closed regions are then used to define the host-wise segmentation $I_{\text{host}} \colon W \to \{0, 1, \ldots\}$ that assigns a unique label to each closed connected component of the host phase that has not been discarded. Voxels corresponding not to these closed connected components are assigned a value of 0. An exemplary cross section of I_{host} is shown in Figure 4(c). A host particle H is defined as the set of voxels given as

$$H = \{x \in W \colon I_{\text{host}}(x) = i\}, \tag{4}$$

for some $i \in \mathbb{N} = \{1, 2, \ldots\}$ such that $H \neq \emptyset$.

To identify individual aggregates, *i.e.*, connected components consisting of guest phase and at least one host, a binary image $I_{\text{GH}} \colon W \to \{0, 1\}$ depicting the union of the guest and host phase is considered, where

$$I_{\text{GH}}(x) = 1 \qquad \text{if and only if} \qquad I_{\text{phase}}(x) \in \{1, 2\} \tag{5}$$

for each $x \in W$. Then, a flood-fill algorithm implemented in *scikit-image* [43] is applied to the image I_{GH} with seed points given by the centers of mass of each previously identified host component. In general, a flood-fill algorithm identifies all voxels that are connected to a given starting voxel. Thus, all voxels of the guest phase that are connected to a certain host are identified. In turn, every voxel of the guest phase that is not reached by the flood-fill algorithm is not attached to any host.

The individual aggregates are then given by connected components that contain at least one host resulting in the aggregate-wise segmentation $I_{\text{agg}} \colon W \to \{0, 1, \ldots\}$, see

Figure 4(d), where an aggregate A is a set of voxels given by

$$A = \{x \in W : I_{\text{agg}}(x) = i\}, \tag{6}$$

for some $i \in \mathbb{N}$ such that $A \neq \emptyset$.

To ensure a robust data base for the statistical analysis of the aggregates in Section 3, additional processing steps are performed that exclude certain aggregates. First, only aggregates A are considered that are completely contained in the cylindrical sampling window W. Consequently, the aggregates intersected by the boundaries of the sampling window are removed.

In addition, aggregates in contact with air inclusions are excluded from the analysis. Since guest particles are non-polar and therefore hydrophobic, they tend to accumulate in the vicinity of air inclusions (see Figure 3). Aggregates comprising guest particles attached to air inclusions are therefore considered artifacts arising from sample embedding rather than from the MF process. More precisely, an aggregate A is removed if for any $x \in A$ there exists a $y \in \mathcal{N}_{26}(x)$ with $I_{\text{phase}}(y) = 3$, where $\mathcal{N}_{26}(x)$ denotes the 26-neighborhood of a voxel $x \in W$ within the sampling window W. Formally $\mathcal{N}_{26}(x)$ is defined as

$$\mathcal{N}_{26}(x) = \{y \in W : |x - y|_{\max} = 1\}$$

with the maximum norm $|z|_{\max} = \max\{|z_1|, |z_2|, |z_3|\}$ for $z = (z_1, z_2, z_3)^\intercal \in \mathbb{R}^3$.

Lastly, aggregates consisting of more than one host particle may appear as connected merely due to the embedding in epoxy. However, reliably separating such aggregates into separate ones containing only a single host particle is challenging. Therefore, these aggregates are also excluded from the analysis and removed. This affects approximately 7 % of the aggregates. A histogram indicating the distribution of the number of hosts per aggregate is shown in Figure S1 in Section S.1 of the supplementary information.

2.4.3 Removing artifacts from sample embedding

Up to this point, an aggregate consists of exactly one host particle along with all connected voxels of the guest phase as described in Section 2.4.2.

In the micro-CT image data, some regions of the guest phase appear to be perpendicularly aligned to the surface of the host particle, as shown by the purple aggregate in Figure 4(d). This results from the mixing of the particles with the epoxy and the random distribution of the free PTFE particles within the matrix. Despite the presence of spacer particles, contact between an already detached PTFE guest particle and a coated host particle may still occur. Therefore, this is an artifact of the sample preparation process that needs to be identified and removed, as it does not reflect the true microstructure of the aggregates. To segment these regions, the tendency of the watershed algorithm to

oversegment non-spherical structures is exploited [45]. The effect should not be confused with contact loss, which refers to the delamination of the (continuous) coating of the host particle, see Figure 3(a).

Each aggregate $A \subset W$ is processed individually. To this end, the binary image $I_A \colon W \to \{0, 1\}$ is considered, which is for all $x \in W$ defined by $I_A(x) = 1$ if and only if $x \in A$. Then, a morphological closing [44] is applied to I_A using a spherical structuring element with a radius of five voxels to fill small gaps between barely non-connected regions of A. This operation primarily closes the gaps associated with contact loss, *i.e.*, between the host particle and the tangentially aligned guest regions.

The Euclidean distance maps of the resulting closed images are subsequently processed using morphological reconstruction [46, 47] to regulate over-segmentation. The severity of the morphological reconstruction algorithm is controlled by a parameter $\alpha \in (0, 1)$, for which a small value of $\alpha = 0.05$ was chosen. Subsequently, a watershed algorithm [48] is applied on each of the processed images, providing a segmented image of each agglomerate. Finally, this image is multiplied voxel-wise with the original binary image I_A of the considered agglomerate in order to reclassify those voxels as pore phase that have been assigned to the foreground by the morphological closing.

In this way, the resulting segmentation of the binary aggregate image I_A would have one large component including the host particle and parts of the guest phase that are in close contact with it. The remaining components would describe parts of the guest phase that are only loosely coated and have partially separated from the host particle. Thus, if a region of the final resulting segmented image does not contain any voxels that belong to the host phase (as given by I_{phase}), then all voxels of that region are classified as an artifact resulting from sample embedding. All remaining voxels of the guest phase (as given by I_{phase}) are classified as belonging to the guest layer of the aggregate A, denoted by $G_{\|}$. Figures 4(d) and 4(e) show 2D cross sections of agglomerate-wise segmentation, with and without guest regions classified as resulting from embedding artifacts. The differences between these two images are shown in Figure 4(f). For the remainder of the manuscript, an aggregate A consists only of the union of its host particle H and its guest layer $G_{\|}$, while neglecting the here identified regions of the guest phase that are considered as artifacts from sample embedding.

2.5 Geometric descriptors

To quantify the structural properties of individual aggregates, the following geometric descriptors are introduced, which reduce the complex 3D morphology of an aggregate to single numbers. The values of these descriptors are used in Section 3 for a comprehensive statistical analysis of the aggregate-wise segmented image data.

As already stated in Sections 2.4.2 and 2.4.3, let $A \subset W$ denote an aggregate consisting

of exactly one host $H \subset A$ and its corresponding guest layer $G_\parallel \subset A$, where $A = H \cup G_\parallel$. Although A, H and $G_\parallel$ are discrete subsets of W derived from three-dimensional image data, they are treated as subsets of a continuous domain for the definition of the following geometric descriptors. In addition, the approximate computation of these descriptors based on discrete sets derived from three-dimensional image data is outlined.

Volume-equivalent diameter. Let $S \subset \mathbb{R}^3$ be a connected set. Then, the size of S is characterized by its volume-equivalent diameter $d_3(S)$, defined as the diameter of a sphere having the same volume as S, that is,

$$d_3(S) = \sqrt[3]{\frac{6\,\nu_3(S)}{\pi}}, \tag{7}$$

where $\nu_3(S)$ denotes the volume of S, which in all practically relevant cases is given by the three-dimensional Lebesgue measure of S [49]. Note that for discrete image data, the volume $\nu_3(S)$ is estimated by counting the number of voxels of $S \cap \mathbb{Z}^3$. In the present study, the volume-equivalent diameter is determined for each aggregate A and its host particle H of the aggregate-wise segmented image data, where it is always assumed that $\nu_3(A) > 0$.

Volume fraction. The (host) volume fraction $\varphi(H)$ of H with respect to A is defined as

$$\varphi(H) = \frac{\nu_3(H)}{\nu_3(A)} \in [0, 1], \tag{8}$$

which quantifies the volumetric proportion of the host phase within the aggregate.

Coating thickness. Without loss of generality, let the center of mass of a host particle H be aligned with the origin. For a direction $v \in \mathbb{S}_2 = \{x \in \mathbb{R}^3 \colon |x| = 1\}$, where $|\cdot|$ denotes the Euclidean norm in $\mathbb{R}^3$, a ray is defined as

$$\gamma_v = \{cv \in \mathbb{R}^3 \colon c > 0\}. \tag{9}$$

For each direction $v \in \mathbb{S}_2$ the point of intrusion $x^{(\mathrm{in})}_{\mathrm{coat}}(v) \in \mathbb{R}^3$ and the point of protrusion $x^{(\mathrm{out})}_{\mathrm{coat}}(v) \in \mathbb{R}^3$ of γ_v with respect to $G_\parallel$ are defined as

$$x^{(\mathrm{in})}_{\mathrm{coat}}(v) = \begin{cases} \operatorname{argmin}_{x \in \gamma_v \cap G_\parallel} |x|, & \text{if } \gamma_v \cap G_\parallel \neq \emptyset, \\ 0, & \text{else,} \end{cases} \tag{10}$$

and

$$x_{\mathrm{coat}}^{(\mathrm{out})}(v) = \begin{cases} \operatorname{argmax}_{x \in \gamma_v \cap G_\parallel} |x|, & \text{if } x \in \gamma_v \cap G_\parallel \neq \emptyset, \\ 0, & \text{else.} \end{cases} \tag{11}$$

Then, the (directional) coating thickness $\delta_{\mathrm{coat}}(v) \geq 0$ in direction $v \in \mathbb{S}_2$ is given by

$$\delta_{\mathrm{coat}}(v) = |x_{\mathrm{coat}}^{(\mathrm{out})}(v) - x_{\mathrm{coat}}^{(\mathrm{in})}(v)|, \tag{12}$$

see Figure 5. For numerical approximations, let V be a set of 1000 equidistant points on $\mathbb{S}_2$, derived by Fibonacci's algorithm [50]. The **mean coating thickness** $\delta_{\mathrm{coat}} > 0$ is then determined by

$$\delta_{\mathrm{coat}} = \frac{1}{\#V_+^{(\mathrm{coat})}} \sum_{v \in V_+^{(\mathrm{coat})}} \delta_{\mathrm{coat}}(v). \tag{13}$$

Here, # denotes cardinality and $V_+^{(\mathrm{coat})} = \{v \in V \colon \delta_{\mathrm{coat}}(v) > 0\}$, where we assume that $\#V_+^{(\mathrm{coat})} > 0$. Thus, δ_{coat} is the mean coating thickness conditioned on the directions in which the coating actually exists. Furthermore, the **coefficient of variation of the coating thickness** $\mathrm{CV}_{\mathrm{coat}} \geq 0$ is defined as

$$\mathrm{CV}_{\mathrm{coat}} = \frac{\sigma_{\mathrm{coat}}}{\delta_{\mathrm{coat}}}, \tag{14}$$

where σ_{coat} denotes the standard deviation of coating thickness that is given as

$$\sigma_{\mathrm{coat}} = \sqrt{\frac{1}{\#V_+^{(\mathrm{coat})}} \sum_{v \in V_+^{(\mathrm{coat})}} \big(\delta_{\mathrm{coat}}(v) - \delta_{\mathrm{coat}}\big)^2}. \tag{15}$$

Note that the coefficient of variation $\mathrm{CV}_{\mathrm{coat}}$ can be considered as normalized standard deviation which quantifies the extent of the relative variability of the coating thickness. The case of $\mathrm{CV}_{\mathrm{coat}} = 1$ indicates that the values of $\delta_{\mathrm{coat}}(v)$ fluctuate within the same order of magnitude as the mean value δ_{coat}.

Surface area coverage (SAC). Let V and $V_+^{(\mathrm{coat})}$ be the sets defined above. Then, the surface area coverage $\theta_{\mathrm{SAC}} \in [0, 1]$ can be approximated by

$$\theta_{\mathrm{SAC}} = \frac{\#V_+^{(\mathrm{coat})}}{\#V}. \tag{16}$$

Note that the case of $\theta_{\mathrm{SAC}} = 1$ corresponds to a fully covered host particle, whereas decreasing values of θ_{SAC} indicate a reduced surface area coverage by the guest phase, see

Figure 5.

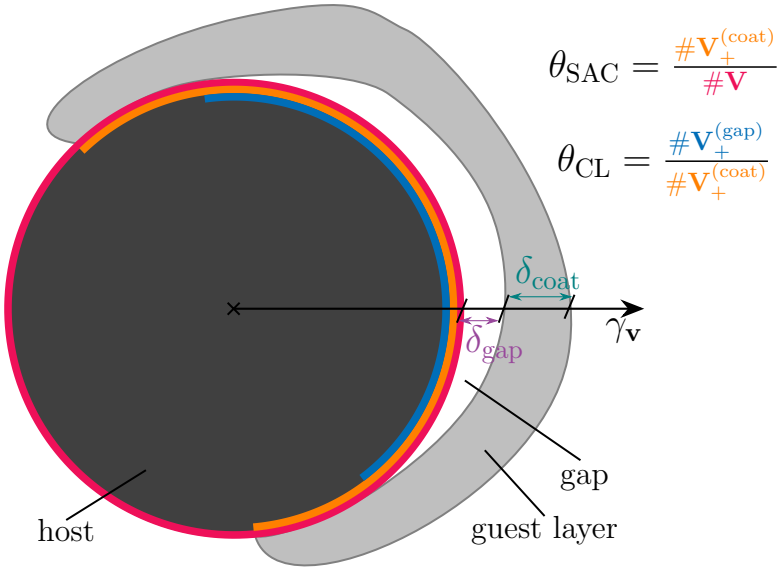

Figure 5: Sketch of directional coating thickness $\delta_{\mathrm{coat}}(v)$, SAC θ_{SAC}, directional gap thickness $\delta_{\mathrm{gap}}(v)$, and contact loss θ_{CL}.

Gap thickness. To quantify the gap between host and guest phase, let for a direction $v \in \mathbb{S}_2$ the point of protrusion $x_{\mathrm{host}}^{(\mathrm{out})}(v) \in \mathbb{R}^3$ of γ_v with respect to the host particle H be defined as

$$x_{\mathrm{host}}^{(\mathrm{out})}(v) = \begin{cases} \operatorname{argmax}_{x \in \gamma_v \cap H} |x|, & \text{if } \gamma_v \cap H \neq \emptyset, \\ 0, & \text{else,} \end{cases} \tag{17}$$

where γ_v is defined as in Eq.(9). The (directional) gap thickness $\delta_{\mathrm{gap}}(v) \geq 0$ in direction $v \in \mathbb{S}_2$ is given by

$$\delta_{\mathrm{gap}}(v) = \begin{cases} |x_{\mathrm{coat}}^{(\mathrm{in})}(v) - x_{\mathrm{host}}^{(\mathrm{out})}(v)|, & \text{if } x_{\mathrm{coat}}^{(\mathrm{in})}(v) \neq 0, \\ 0, & \text{else,} \end{cases} \tag{18}$$

where $x_{\mathrm{coat}}^{(\mathrm{in})}$ denotes the point of intrusion with respect to $G_{\|}$ as introduced in Eq. (10), see Figure 5. The **mean gap thickness** δ_{gap} can be approximated by

$$\delta_{\mathrm{gap}} = \frac{1}{\#V_+^{(\mathrm{gap})}} \sum_{v \in V_+^{(\mathrm{gap})}} \delta_{\mathrm{gap}}(v), \tag{19}$$

with $V_+^{(\mathrm{gap})} = \{v \in V \colon \delta_{\mathrm{gap}}(v) > 0\}$ assuming that $\#V_+^{(\mathrm{gap})} > 0$, where V denotes the set of 1000 equidistant points on $\mathbb{S}_2$ introduced above. Analogously to the coating thickness,

the **coefficient of variation of the gap thickness** $\mathrm{CV}_{\mathrm{gap}} \geq 0$ is defined as

$$\mathrm{CV}_{\mathrm{gap}} = \frac{\sigma_{\mathrm{gap}}}{\delta_{\mathrm{gap}}}, \tag{20}$$

where σ_{gap} denotes the standard deviation of gap thickness, given by

$$\sigma_{\mathrm{gap}} = \sqrt{\frac{1}{\#V_+^{(\mathrm{gap})}} \sum_{v \in V_+^{(\mathrm{gap})}} \left(\delta_{\mathrm{gap}}(v) - \delta_{\mathrm{gap}}\right)^2}. \tag{21}$$

Contact loss. Let $V_+^{(\mathrm{coat})}$ and $V_+^{(\mathrm{gap})}$ be the sets defined above . Then the contact loss θ_{CL} is given by

$$\theta_{\mathrm{CL}} = \frac{V_+^{(\mathrm{gap})}}{V_+^{(\mathrm{coat})}}. \tag{22}$$

It is important to note that the contact loss θ_{CL} depends on the SAC θ_{SAC}. In particular, $\theta_{\mathrm{CL}} = 1$ indicates that, in every direction where coating is present, a gap exists between the host and the coating. Furthermore, if $\theta_{\mathrm{SAC}} = \theta_{\mathrm{CL}} = 0.5$, half of the host particle surface is coated, and in half of the coated regions a gap occurs between the host and the coating. The concept of contact loss is sketched in Figure 5.

3 Results and discussion

As described in Section 2, two disjoint cylindrical regions of an epoxy sample were imaged using micro-CT. These regions contain dry coated aggregates, which were segmented using the procedure outlined in Section 2.4. In the following, the geometric descriptors introduced in Section 2.5 are determined and discussed for these segmented aggregates. The distributions of the descriptors are visualized using number-weighted probability density functions estimated by kernel density estimation, as implemented in the python package seaborn [51]. In particular, only aggregates that are entirely contained within the observation window and contain exactly one host particle are considered. Since both cutouts originate from the same sample, the aggregates segmented from both images are treated as a single data set comprising 174 aggregates.

Figure 6(a) presents the probability densities of the **volume-equivalent diameters** of aggregates and individual hosts. The probability density of the volume-equivalent diameters of individual hosts has its mode at approximately 23 µm, whereas the density of volume-equivalent diameters of aggregates has its peak at 26 µm. The volume of an aggregate is determined as the sum of the volumes of its corresponding host and guest phase.

The probability density of the host **volume fraction** shown in Figure 6(b) exhibits a broad plateau for values from 0.7 to 1, implying that a typical aggregate consists of approximately 70 %–100 % host phase by volume. For reference, the dashed line in Figure 6(b) shows the probability density of host volume fractions under the assumption that every host particle is fully covered by a guest layer with a constant coating thickness of 7.5 µm. The resulting distribution can be interpreted as a lower theoretical boundary for any possible distribution of host volume fractions resulting from an MF process with the here defined process parameters. The mode is at around 0.22, which is drastically lower than the observed host volume fractions. This is because PTFE particles of median diameter 7.5 µm would need to deform in order to create a continuous layer, which reduces the overall thickness of the coating. Furthermore, a portion of the PTFE particles does not contribute to the firmly adhering coating layer, resulting in higher values of observed host volume fractions. See Section S.3 of the supplementary information for more information. This is in part due to the fact that the host particle sizes assume a broad distribution, which is not taken into account in the weight ratio calculation in Equation (1) and again, all PTFE particles would need to be coated on the hosts. At this point, it is not yet apparent how the coating is distributed among the host particles and whether this distribution depends on, *e.g.*, the host particle diameter. This, too, influences the host volume fraction in each aggregate. Therefore, different relationships between geometric descriptors of host particles and the guest phase will be investigated later on.

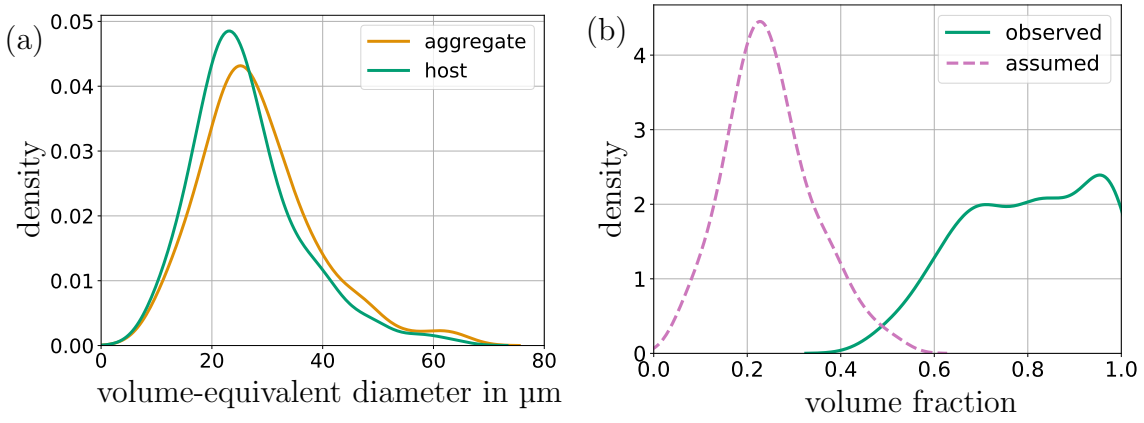

Figure 6: Univariate probability densities of the volume-equivalent diameters of aggregates, hosts as well as the guest layer phase (a), along with the density of the host volume fraction (b). Additionally, the dashed line in (b) indicates the expected host volume fraction under the assumption of full coverage with a constant coating thickness of 7.5 µm.

Figure 7(a) shows the probability densities of the **SAC** and the **contact loss**. From this, one can observe that the SAC is nearly uniformly distributed on the interval [0,1], with a slight increase for values around 0.1. For SE coating of CAM in battery materials, higher SACs, *e.g.*, just under 100 % [52], are targeted and intended to provide a large and

homogeneous ion-conductive interface around the CAM particles. However, sometimes only values between 30 % to 67 % can be achieved [53], depending on the type of coating or mixing process.

In contrast, the contact loss distribution exhibits a peak at approximately 0.53, indicating that roughly half of the coating layer is delaminated from the host particle. The mean value of the contact loss is approximately 0.46, indicating that, on average, about half of the coating is directly attached to the host, while a gap is present between the host and the remaining half of the coating. Note that the probability density is relatively broad and decreases toward larger values. This decline is intuitive, as a value of 1 would correspond to a "floating" coating that is completely detached from the host. Generally, the occurrence of contact loss in the particle system under investigation is likely related to PTFE's chemical nature. PTFE shows weak intrinsic adhesion tendencies to other materials due to its low surface energy and therefore low Hamaker constant (3.8×10^{-20} J [54], whereas that of alumina is 15×10^{-20} J [55]). The surface is smooth, has a low coefficient of friction, and is chemically inert [56]. Consequently, its dry coating mechanism is mainly governed by mechanical interlocking (form-fit), viscoelasticity, and plastic deformation, with creep and stress relaxation representing key time- and temperature-dependent deformation phenomena [57]. Plastic deformation can also contribute to cold sintering or to the so-called room temperature pressure sintering of solid electrolytes. In these processes, high compressive stresses at temperatures well below the thermal sintering temperature can promote neck formation between individual particles, reducing interparticle boundaries and voids and thereby leading to densification [58]. If the PTFE deforms but does not fully conform to the host particle surface, cracks and pores of alumina might be bridged, and the interface contains voids where no adhesion occurs.

Another possible factor that should be considered is the thermal exposure of the materials during the MF process. During MF, the local temperature at the host–guest interface can reach up to 300 °C [59]. PTFE and alumina differ strongly in their thermal expansion behavior. For PTFE, thermal expansion coefficients of $57\,\mu m\,m^{-1}\,K^{-1}$ to $170\,\mu m\,m^{-1}\,K^{-1}$ are reported in the range of 30 °C to 300 °C [60], whereas alumina exhibits much lower values of $5.5\,\mu m\,m^{-1}\,K^{-1}$ to $7.9\,\mu m\,m^{-1}\,K^{-1}$ in a similar temperature range [61]. Based on these material properties, PTFE may undergo stronger expansion-contraction response than the alumina host during heating and subsequent cooling. However, the exact stage at which contact loss occurs, as well as the local thermal and mechanical conditions during coating formation, are not known. Therefore, the thermal expansion mismatch is not proposed here as a direct explanation for the observed contact loss, but rather as a possible contributing factor that can influence the stability of film-like PTFE coatings formed during MF. Similar considerations have been discussed for hot-melt coating systems, where contact loss has been observed and hypothesized to be related to differences in the thermal expansion behavior of the host particle and coating material [62].

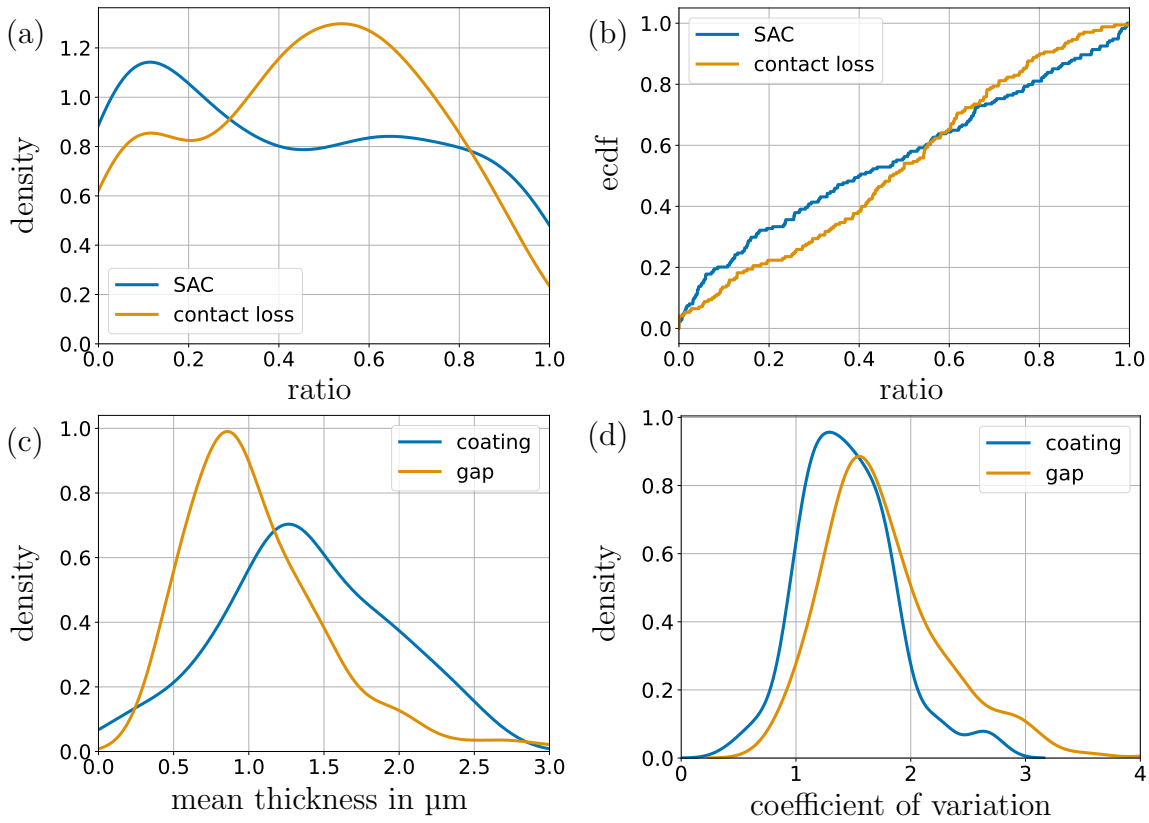

Figure 7: Univariate probability densities of SAC and contact loss (a), mean coating and gap thickness (c), as well as the coefficient of variation of the coating and gap thickness (d), along with the empirical cumulative distribution function of SAC and contact loss (b).

In Figure 7(b), the distributions of SAC and contact loss are additionally represented by empirical cumulative distribution functions (ECDFs), enabling direct quantification of the fraction of host particles that do not exceed a given SAC or contact loss value. Note that, in principle, Figure 7(a) and 7(b) show the same information, only visualized differently. For the SAC, only approximately 20 % of the hosts exhibit SAC ≤ 0.1, whereas about 80 % show SAC ≤ 0.8. The ECDF corresponding to the contact loss quantifies the fraction of host particles whose coating delaminates up to a specified level. For example, approximately 40 % of the hosts exhibit a contact loss of at least 40 %. It is important to consider both descriptors, as it is not only the SAC that determines the battery materials' transport properties but also the fraction of direct solid-solid contact between the CAM and the SE, *i.e.*, any coated surface area not affected by contact loss. The bivariate probability density of contact loss and SAC is presented in Figure S2(c) of the supplementary information.

In the range of 70 % to 100 % SAC, simulations of individual CAM particles revealed no negative effects on the diffusion behavior of lithium ions [53], whereas for SAC<30 %, lithium ions are forced to diffuse over longer distances within the CAM particle, resulting

in concentration gradients and incomplete CAM utilization. Note that this refers to the packed particle state of the electrode, in which even an uncoated surface of one CAM particle after MF can come into contact with the coated surface of another CAM particle, thereby significantly increasing the proportion of host-coating contacts, *i.e.*, CAM-SE contacts. For the current model particle system, in which approximately 70 % of the aggregates have a SAC greater than 20 %, a good SE network can already be achieved and is expected to produce sufficient contacts in the packed state. It should be noted that the MF processing settings (rotational speed, processing time) for the investigated material system have not yet been fully optimized. Therefore, the occurrence of contact loss could be reduced by adapting the mentioned process parameters. The reduction of contact loss will allow for more contacts between the SE and the CAM, which will be available as effective conduction routes, *i.e.*, an efficient SE network. The characteristics of the contact loss (*e.g.*, gap thickness) and its relationship with other coating descriptors will be analyzed in the following. Additionally, the influence of the host particle morphology on these descriptors is examined as well. The purpose of this analysis also lies in identifying possible causes of contact loss.

Figure 7(c) shows the probability densities of the **mean coating thickness** and the **mean gap thickness**. The values of the mean coating thickness vary around 1.5 µm, which is significantly smaller than the median guest particle size of 7.5 µm before MF. This discrepancy is attributed to the strong deformation of the PTFE guest phase during MF. The distribution of the mean gap thickness varies, has its mode at around 1 µm, and is slightly positively skewed, indicating the frequent occurrence of large gaps.

Figure 7(d) shows the probability densities of the **coefficients of variations** of coating and gap thickness. In both cases, the coefficient of variation predominantly assumes values between 1 and 2, which indicates variations of the coating and gap thickness within each aggregate in the order of up to twice the corresponding mean coating and gap thickness.

Since it is well known that the particle size significantly influences the dry coating process [63, 64], the statistical relationship between volume-equivalent diameter and other descriptors is investigated by means of bivariate probability densities. Such multivariate distributions are essential for a detailed characterization of particle processes, as they allow for considering correlations between different geometric rather than evaluating each descriptor separately [65]. Additionally, Table S1 of the supplementary information presents the pairwise Spearman correlation coefficient between all descriptors. It is important to note that all volume-equivalent diameters discussed in the following refer to the size of the host particle.

The bivariate densities relating the volume-equivalent diameter to the SAC, contact loss, and host volume fraction all exhibit a positive correlation, see Figure 8. This implies that larger hosts typically show a higher SAC, exhibit larger gaps between the host and

coating, and have a higher proportion of host within the aggregate. This corresponds to the literature, where a larger particle size ratio between host and guest particles prior to the MF process is associated with more successful coating [63], *i.e.*, larger host particles are more likely to achieve higher SAC values. However, when the guest particle is deformable, which is the case for PTFE, the size ratio becomes less relevant [64]. This is in line with the observation that there is only a slight positive correlation between the volume-equivalent diameter and SAC, see Figure 8(a).

Furthermore, the contact loss is positively correlated with the host particle size (see Figure 8(b)). One possible explanation is that larger host particles exhibit a lower surface curvature. Consequently, the already flattened PTFE particles may undergo less additional deformation upon attachment, potentially reducing the degree of mechanical interlocking between the coating and the host surface. In addition, larger host particles can generate higher collision-induced stresses due to their greater mass. These stresses may promote delamination in weakly attached coating regions, thereby increasing contact loss.

The positive correlation between the volume-equivalent diameter and both the SAC and the host volume fraction (Figure 8(a), 8(c)) may appear contradictory, as an increasing SAC typically implies a larger guest phase and thus a lower host volume fraction.

However, while both quantities are positively correlated with the volume-equivalent diameter, they are negatively correlated with each other (see Figure S2(b)). Thus, while larger host particles typically exhibit larger SAC values than smaller host particles, the volume of their guest phase does not increase proportionally to the volume of the host particle.

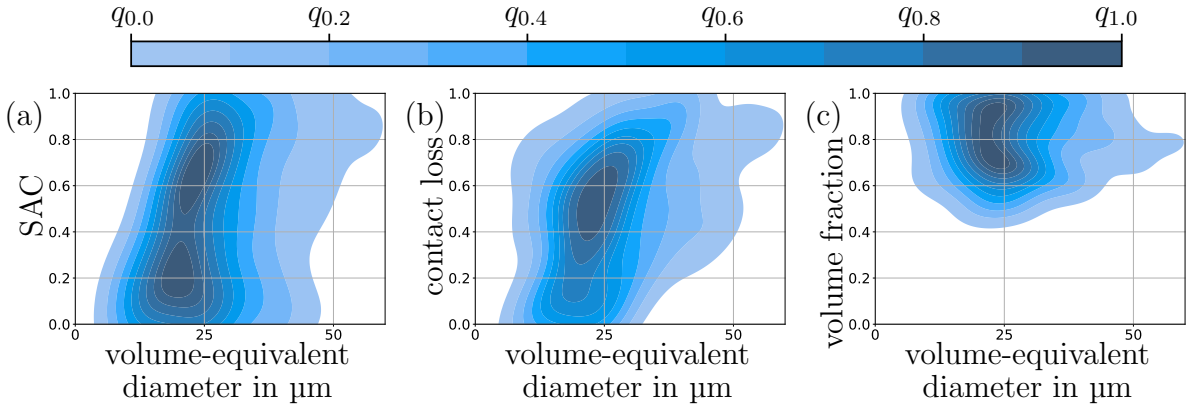

Figure 8: The bivariate probability densities between host volume-equivalent diameter and SAC (a), contact loss (b) as well as host volume fraction (c) exhibit a positive correlation structure. The shading of the colors indicate different quantiles of the probability densities, where q_p denotes the p-quantile.

Figure 9(a) and 9(c) (and the corresponding correlation coefficients as shown in Table S1) imply that large host particles typically have a thicker coating that exhibits a

larger spread in its thickness. A similar behavior is observable for the mean gap thickness in Figure 9(b). However, the coefficient of variation of the gap thickness shows a negative correlation with the volume-equivalent diameter, as seen in Figure 9(d). This indicates that the variations of the gap thickness within each particle decrease in relation to the mean gap thickness for larger host particles. Both effects again show the tendency for coating to be favored on larger host particles. However, several mechanisms may simultaneously contribute to the formation of a thicker and less homogeneously distributed coating.

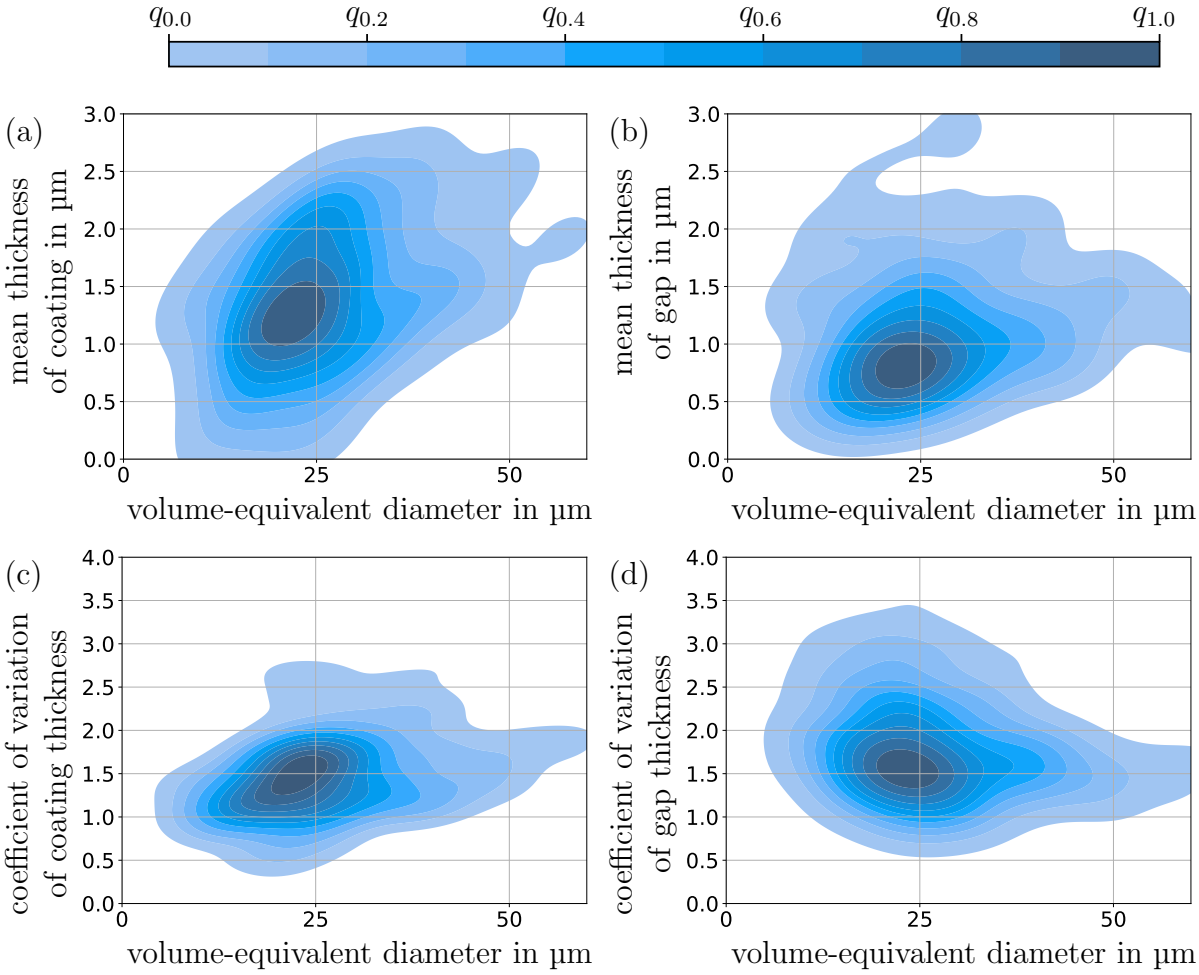

Figure 9: Bivariate probability densities between volume equivalent diameter and mean of coating thickness (a), mean of gap thickness (b), coefficient of variation of coating thickness (c) as well as coefficient of variation of gap thickness (d). The shading of the colors indicate different quantiles of the probability densities, where q_p denotes the p-quantile.

In addition to correlations with the host volume-equivalent diameter, the relationship between SAC and other descriptors was investigated in more detail. Since Figure 8(a) indicates that SAC is positively correlated with host particle size, the correlations between SAC and the remaining descriptors were analyzed separately for two aggregate size classes. One class contains aggregates whose host particles have a volume-equivalent diameter

smaller than or equal to the median ($\approx 24.2\,\mu m$), while the other contains the remaining aggregates. By definition of the median, this subdivision results in two classes with an equal number of 87 aggregates each. For completeness, the mean volume-equivalent diameter of the host particles based on the micro-CT data is $\approx 26.2\,\mu m$. The Spearman correlation coefficients between the SAC and other descriptors are reported in Table 1 for both small and large host particles. Corresponding bivariate probability densities are provided in Section S.2 of the supplementary information.

	θ_{SAC} (small)	θ_{SAC} (large)
d_3	0.422	0.066
φ	-0.599	-0.899
θ_{SAC}	1.000	1.000
θ_{CL}	0.357	0.518
δ_{coat}	0.519	0.679
δ_{gap}	-0.061	-0.017
CV_{coat}	0.699	0.723
CV_{gap}	-0.105	-0.191

Table 1: Pairwise Spearman correlation coefficients between SAC and selected descriptors for two size classes. One class (small) contains aggregates whose host particles are smaller than or equal to the median volume-equivalent diameter of $\approx 24.2\,\mu m$, while the other (large) contains the remaining aggregates. Blue indicates positive correlation, while red represents negative correlation. The intensity of the color reflects the strength of the correlation.

When the two size classes are considered separately, a strong correlation between volume-equivalent diameter and SAC is observed for aggregates containing small hosts, whereas the correlation for aggregates with large hosts vanishes. This is likely due to the fact that aggregates within the group of large hosts already exhibit high SAC values independent of their exact size. On the other hand, aggregates within the group of small hosts show a wider range of SAC values that heavily depend on their exact size, see also Figure 8(a).

A negative correlation between SAC and host volume fraction is observable, see Table 1. Under the condition of a relatively constant coating thickness, such a relation is intuitive since a higher SAC typically results in a higher guest phase volume, which reduces the host volume fraction. The negative correlation between SAC and the host volume fraction is clearly stronger for aggregates containing large particles. However, this effect may largely be driven by the previously discussed correlation between host particle size and volume fraction. The remaining correlations show only minor changes between the two size classes and should be interpreted cautiously.

In particular, the SAC is positively correlated with contact loss, indicating that highly covered hosts tend to have less attachment or close contact to their guest coating. De-

lamination may spread through the PTFE coating due to the transfer of internal stresses upon collisions. Once detached, the coating layer (a single PTFE composite) will likely no longer adhere locally to the alumina surface. The weaker correlation observed for small hosts may be related to their generally smaller SAC values, see Figure 8(a). From a mechanistic perspective, this is reasonable, as a low SAC combined with a high contact loss would imply a coating that is only weakly attached to the particle. In addition, a strong correlation between the mean coating thickness and the contact loss is observed (Spearman correlation coefficient of 0.856, see Table S1 of the supplementary information). This effect may be attributed to the above mentioned increased shear stress acting on coating structures with a higher variability in their coating thickness.

SAC also shows a positive correlation with the mean coating thickness and the coefficient of variation of the coating thickness. These correlations are more pronounced for aggregates containing larger host particles. This may be related to the generally larger SAC values observed for larger hosts, which tend to result in thicker coatings and greater variability in coating thickness.

In contrast, host particle size appears to have little influence on the relationship between SAC and gap properties. The correlation coefficients between SAC and both the mean gap thickness and the coefficient of variation of the gap thickness are close to zero for both size classes.

4 Conclusion

A particle system consisting of a model CAM (alumina host particle) and a model SE (PTFE guest particle) was processed into coated hetero-aggregates using MF. Subsequently, the hetero-aggregates were embedded in epoxy and imaged using micro-CT measurements. Several image processing techniques were applied to obtain a particle-discrete segmentation that subdivides each hetero-aggregate into its host and guest phase. Based on the segmented image data, various geometric descriptors that characterize the morphology of the hetero-aggregate were determined, in particular with respect to the thickness, SAC, and structural connectivity of the coating layer on the host particle surface, as these aspects play a crucial role in influencing the macroscopic properties, *i.e.*, the electrochemical performance of hetero-aggregates in battery systems. Using methods of multivariate statistical analysis, the joint distribution of these descriptors was investigated, which provides understanding not only of their individual one-dimensional distributions but also of the interdependencies between them.

The applied methods significantly improve our understanding of the behavior of the chosen system during the MF process. In particular, they enable the 3D analysis of the resulting coating structures and allow for their quantitative characterization using appropriate descriptors. Certain phenomena, such as the contact loss between host and

guest particle, would not be detectable nor quantifiable without such 3D approaches.

In future work, the established methods can be applied to other data sets of hetero-aggregates resulting from MF or related processes. For the current, MF processed particle system further experiments will be conducted with varying process parameters, such as rotational speed or overall process time, in order to optimize SAC and contact loss behavior. As a consequence, the presented statistical framework facilitates revealing process-structure relationships, which is crucial for optimizing the results of the coating process.

Funding

The funding of this work as part of the priority program 2289 "Hetero-aggregates" (grant number: 462365306) by the German Research Foundation (DFG) is gratefully acknowledged.

Acknowledgments

The authors would like to thank A. Kästner for laser diffraction measurements of the pristine materials, Dr. G. Schmidt for acquisition of the SEM images of the non-embedded pristine and coated particles and Mrs. C. Ludewig for the support during sample re-embedding and polishing.

Data availability

Raw reconstructed and segmented micro-CT (alumina and PTFE phase) as well as all high-resolution SEM images and the trained ilastik segmentation model can be found in the open access repository of Saxon Universities (OPARA) under the following DOI `https://doi.org/10.25532/OPARA-1322`.

References

[1] T. Yokoyama, K. Urayama, M. Naito and M. Kato. The angmill mechanofusion system and its applications. *KONA Powder and Particle Journal*, 5:59–68, 1987.

[2] R. Pfeffer, R. N. Dave, D. Wei and M. Ramlakhan. Synthesis of engineered particulates with tailored properties using dry particle coating. *Powder Technology*, 117: 40–67, 2001.

[3] Q. T. Zhou and D. A. Morton. Drug-lactose binding aspects in adhesive mixtures:

controlling performance in dry powder inhaler formulations by altering lactose carrier surfaces. *Advanced Drug Delivery Reviews*, 64:275–284, 2012.

[4] N. Bungert, M. Kobler and R. Scherließ. In-depth comparison of dry particle coating processes used in DPI particle engineering. *Pharmaceutics*, 13:580, 2021.

[5] I. S. Jeon, M. H. Lee, H.-H. Choi, S. Lee, J. W. Chon, D. J. Chung, J. H. Park and J. Y. Jho. Mechanical properties and bioactivity of polyetheretherketone/hydroxyapatite/carbon fiber composite prepared by the mechanofusion process. *Polymers*, 13:1978, 2021.

[6] B. Sadeghi, G. Fan, Z. Tan, Z. Li, A. Kondo and M. Naito. Smart mechanical powder processing for producing carbon nanotube reinforced aluminum matrix composites. *KONA Powder and Particle Journal*, 39:219–229, 2022.

[7] L. Zheng, T. D. Hatchard and M. N. Obrovac. A high-quality mechanofusion coating for enhancing lithium-ion battery cathode material performance. *MRS Communications*, 9:245–250, 2019.

[8] J. Heo, J. Sung, D.-H. Kim, I. Hwang, S. Kim, J.-H. Park, Y.-J. Lee, H.-Y. Choi, D. Kim and J.-W. Park. Advanced performance through mechanofusion-induced uniform interfacial layers for all-solid-state lithium-sulfur batteries. *Applied Surface Science*, 688:162292, 2025.

[9] W. Jiang, X. Zhu, Y. Liu, S. Zhao, R. Huang, M. Ling, L. Wang and C. Liang. Design of composite cathodes for sulfide-based all-solid-state batteries. *eTransportation*, 17: 100246, 2023.

[10] P. Bunyanidhi and M. Sawangphruk. Improving interfacial contact within solid-state lithium batteries using the composite materials at the cathode produced by a scalable mechanofusion process. *ECS Transactions*, 97:267, 2020.

[11] H. Bockholt, W. Haselrieder and A. Kwade. Intensive powder mixing for dry dispersing of carbon black and its relevance for lithium-ion battery cathodes. *Powder Technology*, 297:266–274, 2016.

[12] D. Hou, J. Han, C. Geng, Z. Xu, M. M. AlMarzooqi, J. Zhang, Z. Yang, J. Min, X. Xiao, O. Borkiewicz, K. Wiaderek, Y. Liu, K. Zhao and F. Lin. Surface coating by mechanofusion modulates bulk charging pathways and battery performance of Ni-rich layered cathodes. *Proceedings of the National Academy of Sciences of the United States of America*, 119:e2212802119, 2022.

[13] C. Khunrugsa, P. Chiochan, F. Duriyasart, C. Jangsan, P. Kullawattanapokin and M. Sawangphruk. Long-term cycling stability of 18650 Li-ion batteries cells using

NMC811 core@shell structure with tetra-materials. *ECS Meeting Abstracts*, MA2021-01:246, 2021.

[14] N. Phattharasupakun, J. Wutthiprom, S. Duangdangchote, S. Sarawutanukul, C. Tomon, F. Duriyasart, S. Tubtimkuna, C. Aphirakaramwong and M. Sawangphruk. Core-shell Ni-rich NMC-nanocarbon cathode from scalable solvent-free mechanofusion for high-performance 18650 Li-ion batteries. *Energy Storage Materials*, 36:485–495, 2021.

[15] M. Kissel, F. Frankenberg, T. Demuth, A. Lai, N. Laser, D. Wagner, A. Eisa, P. Michalowski, K. Volz, A. Kwade and J. Janek. Mechanofusion-derived cathode composite microstructures with scalable mixed conducting matrix coatings for solid state batteries. *Nature Communications*, 17:3215, 2026.

[16] H. Nakamura and S. Watano. Dry coating of electrode particle with solid electrolyte for composite electrode of all-solid-state battery. In K. Kanamura, editor, *Next Generation Batteries*, pages 93–105. Springer, 2021.

[17] M. Clausnitzer, T. Danner, B. Prifling, M. Neumann, V. Schmidt and A. Latz. Influence of electrode structuring techniques on the performance of all-solid-state batteries. *Batteries & Supercaps*, 7:e202300522, 2024.

[18] M. Clausnitzer, R. Mücke, F. Al-Jaljouli, S. Hein, M. Finsterbusch, T. Danner, D. Fattakhova-Rohlfing, O. Guillon and A. Latz. Optimizing the composite cathode microstructure in all-solid-state batteries by structure-resolved simulations. *Batteries & Supercaps*, 6:e202300167, 2023.

[19] J. Park, K. T. Kim, D. Y. Oh, D. Jin, D. Kim, Y. S. Jung and Y. M. Lee. Digital twin-driven all-solid-state battery: Unraveling the physical and electrochemical behaviors. *Advanced Energy Materials*, 10:2001563, 2020.

[20] B. Prifling, L. Fuchs, A. Yessim, M. Osenberg, M. Paulisch-Rinke, P. Zimmer, M. D. Hager, U. S. Schubert, I. Manke, T. Carraro and V. Schmidt. Correlating the 3D morphology of polymer-based battery electrodes with effective transport properties. *ACS Applied Materials & Interfaces*, 16:66571–66583, 2024.

[21] P. Gräfensteiner, M. Osenberg, A. Hilger, N. Bohn, J. R. Binder, I. Manke, V. Schmidt and M. Neumann. Data-driven stochastic 3D modeling of the nanoporous binder-conductive additive phase in battery cathodes. *Journal of Mathematics in Industry*, 15:9, 2025.

[22] A. Dufter, S. Weber, O. Furat, J. Schubert, R. Rekers, M. Luczak, E. Glatt, A. Wiegmann, A. Bielefeld and V. Schmidt. Virtual materials testing of ASSB cathodes

combining AI-based stochastic 3D modeling and numerical simulations. *Materials Today Communications*, 2026. in print.

[23] C. Park, J. Lee, S. Lee, Y. J. Han, J. Kim and S.-K. Jung. Organic–additive–derived cathode electrolyte interphase layer mitigating intertwined chemical and mechanical degradation for sulfide–based solid–state batteries. *Advanced Energy Materials*, 13: 2203861, 2023.

[24] S. C. Sand, J. L. M. Rupp and B. Yildiz. A critical review on Li-ion transport, chemistry and structure of ceramic–polymer composite electrolytes for solid state batteries. *Chem. Soc. Rev.*, 54:178–200, 2025.

[25] S. Hori, K. Suzuki, M. Hirayama and R. Kanno. Crystalline electrolyte. In K. Kanamura, editor, *Next Generation Batteries: Realization of High Energy Density Rechargeable Batteries*, pages 49–60. Springer, 2021.

[26] Q. Zhang, D. Cao, Y. Ma, A. Natan, P. Aurora and H. Zhu. Sulfide-based solid-state electrolytes: Synthesis, stability, and potential for all-solid-state batteries. *Advanced Materials*, 31:1901131, 2019.

[27] D. Li, H. Liu, C. Wang, C. Yan, Q. Zhang, C.-W. Nan and L.-Z. Fan. High ionic conductive, mechanical robust sulfide solid electrolyte films and interface design for all-solid-state lithium metal batteries. *Advanced Functional Materials*, 34:2315555, 2024.

[28] S. Puls, L. Ketter, W. G. Zeier and N. M. Vargas-Barbosa. Opportunities and limitations of partial transport quantification in all-solid-state composite electrodes. *ACS Electrochemistry*, 1:2432–2447, 2025.

[29] R. Amin and Y.-M. Chiang. Characterization of electronic and ionic transport in $Li_{1-x}Ni_{0.33}Mn_{0.33}Co_{0.33}O_2$($NMC_{333}$) and $Li_{1-x}Ni_{0.50}Mn_{0.20}Co_{0.30}O_2$ (NMC_{523}) as a function of Li content. *Journal of The Electrochemical Society*, 163:A1512, 2016.

[30] T. Kawaguchi, H. Nakamura and S. Watano. Parametric study of dry coating process of electrode particle with model material of sulfide solid electrolytes for all-solid-state battery. *Powder Technology*, 305:241–249, 2017.

[31] P. Gräfensteiner, J. Friebel, L. Ditscherlein, O. Furat, U. A. Peuker and V. Schmidt. An AFM-based approach for quantification of guest particle deformation during mechano-fusion. *Powder Technology*, 434:119293, 2024.

[32] Y. Luo, Z. Rao, X. Yang, C. Wang, X. Sun and X. Li. Safety concerns in solid-state lithium batteries: from materials to devices. *Energy & Environmental Science*, 17: 7543–7565, 2024.

[33] J. Zhang, J. Qiao, K. Sun and Z. Wang. Balancing particle properties for practical lithium-ion batteries. *Particuology*, 61:18–29, 2022.

[34] J. M. Friebel, R. Ditscherlein, L. Ditscherlein and U. A. Peuker. Three-dimensional characterization of dry particle coating structures originating from the mechano-fusion process. *Microscopy and Microanalysis*, 30:179–191, 2024.

[35] J. Yang, A. Sliva, A. Banerjee, R. N. Dave and R. Pfeffer. Dry particle coating for improving the flowability of cohesive powders. *Powder Technology*, 158:21–33, 2005.

[36] J. Kim, M. J. Kim, J. Kim, J. W. Lee, J. Park, S. E. Wang, S. Lee, Y. C. Kang, U. Paik, D. S. Jung and T. Song. High–performance all–solid–state batteries enabled by intimate interfacial contact between the cathode and sulfide–based solid electrolytes. *Advanced Functional Materials*, 33:2211355, 2023.

[37] R. Ditscherlein, T. Leißner and U. A. Peuker. Preparation strategy for statistically significant micrometer-sized particle systems suitable for correlative 3D imaging workflows on the example of X-ray microtomography. *Powder Technology*, 395: 235–242, 2022.

[38] S. Berg, D. Kutra, T. Kroeger, C. N. Straehle, B. X. Kausler, C. Haubold, M. Schiegg, J. Ales, T. Beier, M. Rudy, K. Eren, J. I. Cervantes, B. Xu, F. Beuttenmueller, A. Wolny, C. Zhang, U. Koethe, F. A. Hamprecht and A. Kreshuk. ilastik: interactive machine learning for (bio)image analysis. *Nature Methods*, 16:1226–1232, 2019.

[39] J. M. Seyffer, N. Stefenelli, L. Ditscherlein and U. A. Peuker. Guest particle deformation and powder flow behavior in mechano-fusion: Linking microscopic structure to macroscopic performance. *Powder Technology*, 469:121853, 2025.

[40] C. Park, J. Choi, S. Park, H.-J. Kim, Y. Kim, G. Lim, J. Lee, E. Lee, S. Jo, J. Kim, J. Kim, J. Lim, T. Kim, J. Hong, D. Kim and S.-K. Jung. Interfacial chemistry-driven reaction dynamics and resultant microstructural evolution in lithium-based all-solid-state batteries. *Nature Communications*, 16:8838, 2025.

[41] Comet Technologies Canada Inc. Dragonfly, 2024. Version: 2024.1.

[42] O. Ronneberger, P. Fischer and T. Brox. U-net: Convolutional networks for biomedical image segmentation. In N. Navab, J. Hornegger, W. M. Wells and A. F. Frangi, editors, *Medical Image Computing and Computer-Assisted Intervention – MICCAI 2015*, pages 234–241. Springer, 2015.

[43] S. Van der Walt, J. L. Schönberger, J. Nunez-Iglesias, F. Boulogne, J. D. Warner, N. Yager, E. Gouillart and T. Yu. scikit-image: image processing in Python. *PeerJ*, 2:e453, 2014.

[44] P. Soille. *Morphological Image Analysis: Principles and Applications*. Springer, 2004.

[45] J. Zheng and R. D. Hryciw. Segmentation of contacting soil particles in images by modified watershed analysis. *Computers and Geotechnics*, 73:142–152, 2016.

[46] J. Serra. *Image Analysis and Mathematical Morphology*. Academic Press, 1982.

[47] L. Vincent. Morphological grayscale reconstruction: Definition, efficient algorithm and applications in image analysis. In *Proceedings of 1992 IEEE Computer Society Conference on Computer Vision and Pattern Recognition*, pages 633–635. IEEE Computer Society, 1992.

[48] J. B. T. M. Roerdink and A. Meijster. The watershed transform: definitions, algorithms and parallelization strategies. *Fundamenta Informaticae*, 41:187–228, 2000.

[49] A. Klenke. *Probability Theory: A Comprehensive Course*. Springer, 2020.

[50] Á. González. Measurement of areas on a sphere using fibonacci and latitude-longitude lattices. *Mathematical Geosciences*, 42:49–64, 2010.

[51] M. L. Waskom. Seaborn: Statistical data visualization. *Journal of Open Source Software*, 6:3021, 2021.

[52] Y. J. Kim, T. D. Hoang, S. C. Han, J. A. Bang, H. W. Kang, J. Kim, H. Park, J.-H. Park, J.-W. Park, G. Park, Y.-J. Lee, D. Kim, S.-W. Eom, J.-H. Choi, S.-K. Lee, J. Moon, Y.-C. Ha and B. G. Kim. Exploring optimal cathode composite design for high-performance all-solid-state batteries. *Energy Storage Materials*, 71:103607, 2024.

[53] D. Lee, Y. Shim, Y. Kim, G. Kwon, S. H. Choi, K. Kim and D.-J. Yoo. Shear force effect of the dry process on cathode contact coverage in all-solid-state batteries. *Nature Communications*, 15:4763, 2024.

[54] D. B. Hough and L. R. White. The calculation of hamaker constants from liftshitz theory with applications to wetting phenomena. *Advances in Colloid and Interface Science*, 14:3–41, 1980.

[55] L. Bergström, A. Meurk, H. Arwin and D. J. Rowcliffe. Estimation of hamaker constants of ceramic materials from optical data using lifshitz theory. *Journal of the American Ceramic Society*, 79:339–348, 1996.

[56] B. Gupta. 1 - textile fiber morphology, structure and properties in relation to friction. In B. Gupta, editor, *Friction in Textile Materials*, Woodhead Publishing Series in Textiles, pages 3–36. Woodhead Publishing, 2008.

[57] D. W. Van Krevelen and K. Te Nijenhuis. Chapter 13 - mechanical properties of solid polymers. In D. W. Van Krevelen and K. Te Nijenhuis, editors, *Properties of Polymers (Fourth Edition)*, pages 383–503. Elsevier, 2009.

[58] A. Sakuda, A. Hayashi and M. Tatsumisago. Sulfide solid electrolyte with favorable mechanical property for all-solid-state lithium battery. *Scientific Reports*, 3:2261, 2013.

[59] K. Mizota, S. Fujiwara and M. Senna. Microstructure and adhesion mechanism of mechanically prepared composite particles. *Materials Science and Engineering: B*, 10:139–147, 1991.

[60] MatWeb. Polytetrafluoroethylene (PTFE), Molded, 2026-05-28. URL `https://www.matweb.com/search/DataSheet.aspx?MatGUID=4d14eac958e5401a8fd152e1261b6843`.

[61] MatWeb. Corundum, Aluminum Oxide, Alumina, 99.9%, Al_2O_3, 2026-04-10. URL `https://www.matweb.com/search/DataSheet.aspx?MatGUID=c8c56ad547ae4cfabad15977bfb537f1&ckck=1`.

[62] B. Woerthmann, L. Totzauer and H. Briesen. Delamination and wetting behavior of natural hot-melt coating materials. *Powder Technology*, 404:117443, 2022.

[63] K. Zheng, K. Kunnath, Z. Ling, L. Chen and R. N. Davé. Influence of guest and host particle sizes on dry coating effectiveness: When not to use high mixing intensity. *Powder Technology*, 366:150–163, 2020.

[64] M. Naito, A. Kondo and T. Yokoyama. Applications of comminution techniques for the surface modification of powder materials. *ISIJ International*, 33:915–924, 1993.

[65] E. Schach, T. Buchwald, O. Furat, F. Tischer, A. Kaas, L. Kuger, M. Masuhr, J. Sygusch, T. Wilhelm, R. Ditscherlein and U. A. Peuker. Progress in the application of multidimensional particle property distributions: The separation function. *KONA Powder and Particle Journal*, 42:134–155, 2025.

S Supplementary Information

S.1 Image segmentation

Figure S1 shows a histogram indicating the relative frequencies of the number of hosts per aggregate used in the image post processing procedure described in Section 2.4.2. Only aggregates that contain exactly one host are considered for further analysis.

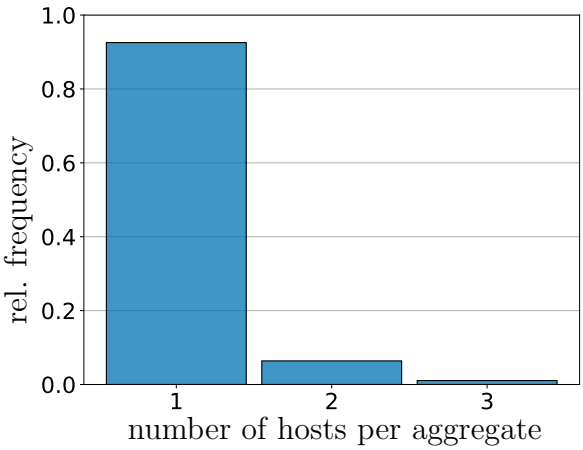

Figure S1: Histogram indicating the relative frequencies of the number of hosts per aggregate.

S.2 Additional correlation coefficients

Since the coating process is significantly influenced by particle size [63, 64], the correlation analysis presented in Section 3 primarily focuses on relationships between the volume-equivalent diameter and other descriptors. For completeness, the Spearman correlation coefficients for all descriptor pairs are reported in Table S1.

	d_3	φ	θ_{SAC}	θ_{CL}	δ_{coat}	δ_{gap}	$\mathrm{CV}_{\mathrm{coat}}$	$\mathrm{CV}_{\mathrm{gap}}$
d_3	1.000	0.155	0.302	0.430	0.409	0.266	0.347	-0.178
φ	0.155	1.000	-0.697	-0.450	-0.515	-0.174	-0.442	0.289
θ_{SAC}	0.302	-0.697	1.000	0.488	0.638	0.009	0.723	-0.203
θ_{CL}	0.430	-0.450	0.488	1.000	0.859	0.623	0.657	-0.338
δ_{coat}	0.409	-0.515	0.638	0.859	1.000	0.551	0.713	-0.436
δ_{gap}	0.266	-0.174	0.009	0.623	0.551	1.000	0.047	-0.563
$\mathrm{CV}_{\mathrm{coat}}$	0.347	-0.442	0.723	0.657	0.713	0.047	1.000	-0.083
$\mathrm{CV}_{\mathrm{gap}}$	-0.178	0.289	-0.203	-0.338	-0.436	-0.563	-0.083	1.000

Table S1: Pairwise Spearman correlation coefficients between all descriptors. Blue indicates positive correlation, while red represents negative correlation. The intensity of the color reflects the strength of the correlation.

Additionally, for interactions between SAC and other descriptors, only the correlation coefficients for two host particle size classes are provided in the main text, see Table 1. For a more detailed insight into the correlation structure of some of these pairs, the bivariate probability densities are shown in Figures S2 and S3.

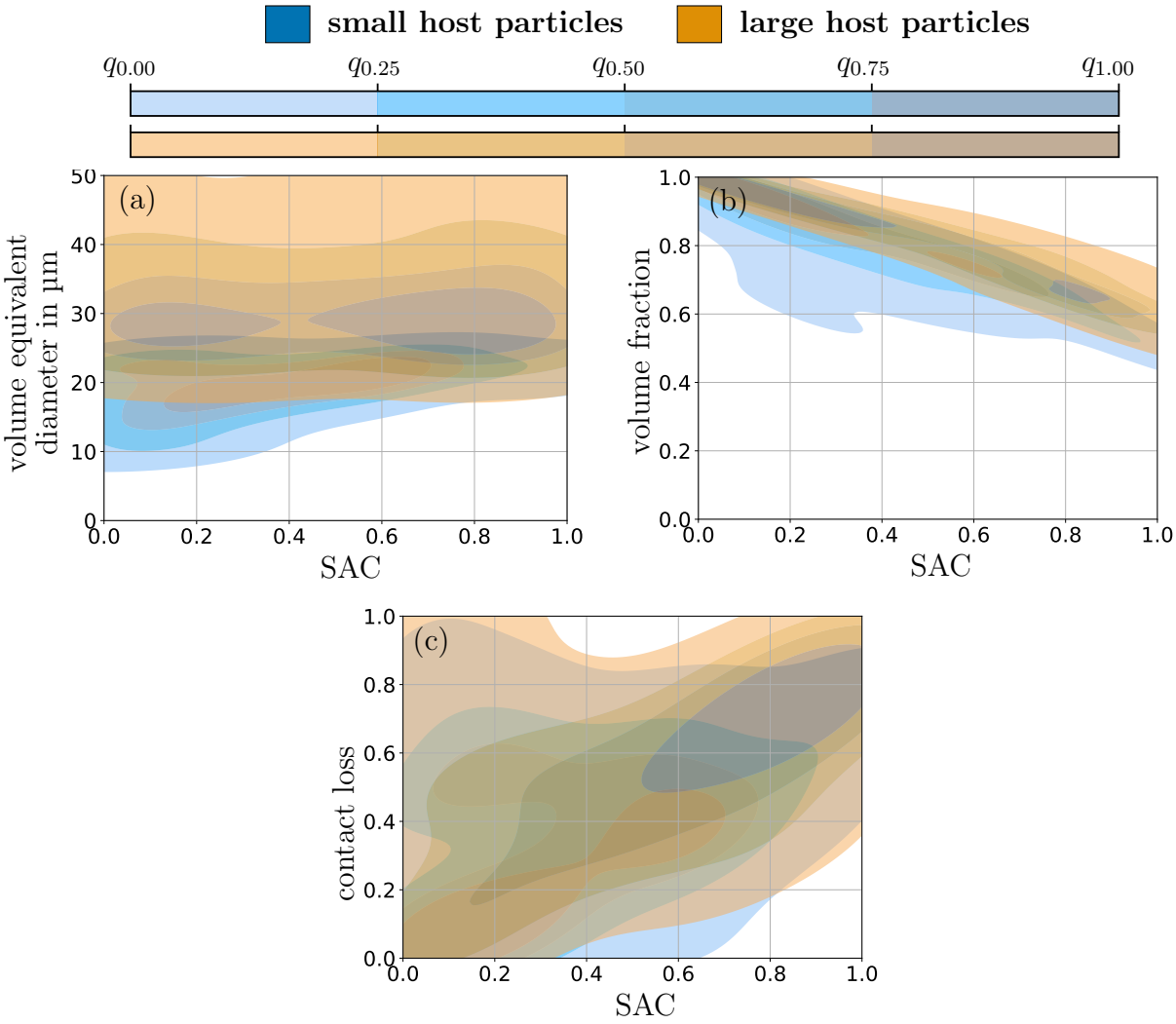

Figure S2: Bivariate probability densities between SAC and volume-equivalent diameter (a), host volume fraction (b) as well as contact loss (c) for two size classes. Blue indicates the density corresponding to aggregates whose host particles have a volume-equivalent diameter smaller than or equal to the median ($\approx 24.2\,\mu m$), while orange represents the density corresponding to the remaining aggregates. The shading of the colors indicate different quantiles of the probability densities, where q_p denotes the p-quantile.

S.3 Attached guest particle fraction

To quantify the quality of the coating process, the fraction of guest particles attached to host particles is determined. Accordingly, the proportion of free guest particles is also evaluated. These originate from PTFE particles that were never incorporated into the

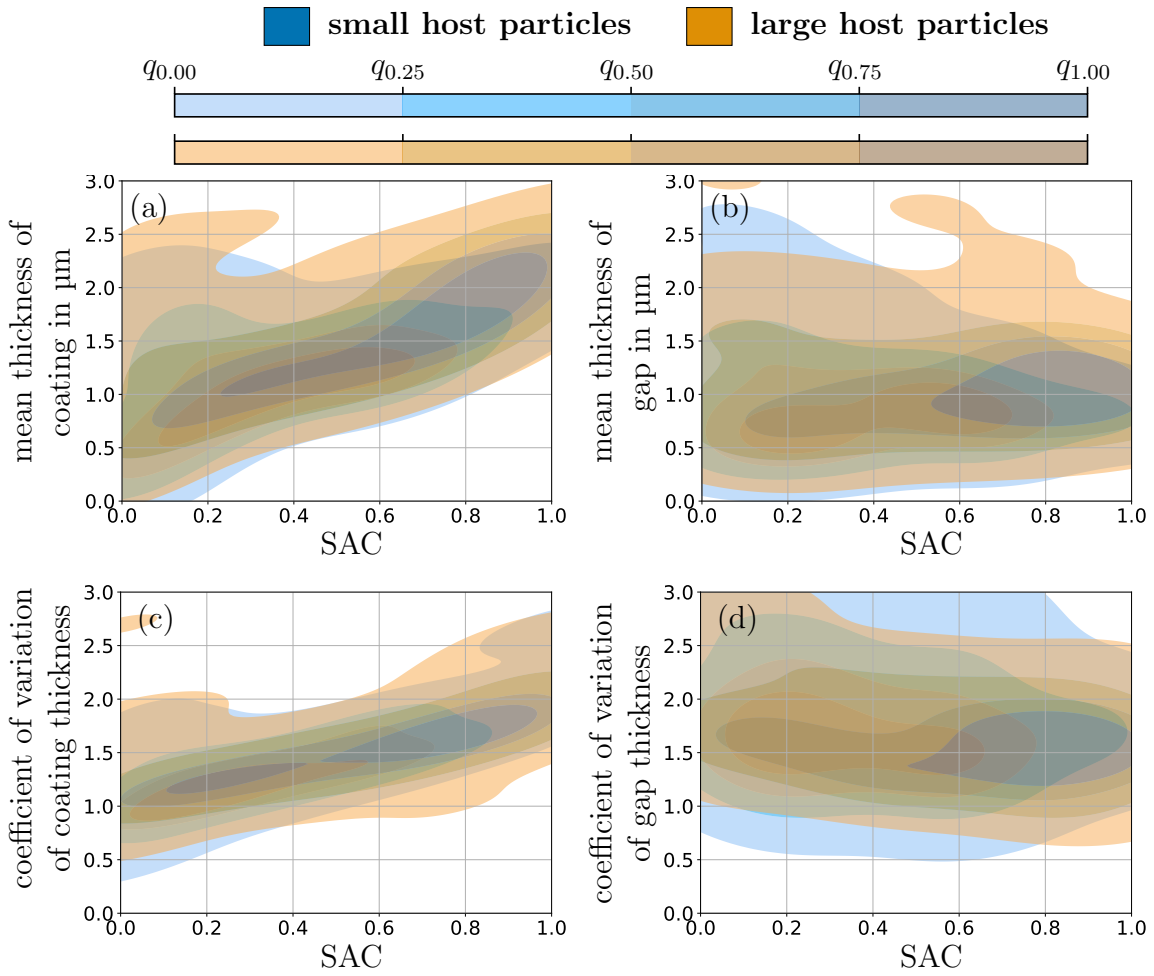

Figure S3: Bivariate probability densities between SAC and mean of coating thickness (a), mean of gap thickness (b), coefficient of variation coating thickness (c) as well as coefficient of variation of gap thickness (d) for two size classes. Blue indicates the density corresponding to aggregates whose host particles have a volume-equivalent diameter smaller than or equal to the median ($\approx 24.2\,\mu m$), while orange represents the density corresponding to the remaining aggregates. The shading of the colors indicate different quantiles of the probability densities, where q_p denotes the p-quantile.

coating during processing and any only weakly adhering PTFE particles (as observed in the SEM images of Figure 1), which are removed during the sample preparation.

The fraction of attached guest particles θ_{att} is given as

$$\theta_{\text{att}} = \frac{|\mathcal{G}_{\parallel}|}{|\mathcal{G}^{\text{all}}|} \in [0, 1], \tag{S1}$$

where $\mathcal{G}_{\parallel}$ denotes the union of the guest layer phase corresponding to any aggregate A.

Note that, for the determination of θ_{att}, all aggregates A are considered. This includes aggregates containing more than one host particle, aggregates in contact with air inclusions, and aggregates not entirely contained within the observation window. To detect the regions of the guest phase that appear as connected as a result from sample embedding,

the procedure outlined in Section 2.4.3 is conducted. However, applying this algorithm to aggregates in contact with air inclusions or containing multiple host particles may introduce a bias, leading to an overestimation of the guest layer. In the case of aggregates adjacent to air inclusions, guest phase regions attached to the inclusion rather than to the host may be incorrectly assigned to the guest layer. Moreover, since the detection algorithm is designed for aggregates containing a single host particle, its application to multi-host aggregates may result in guest regions being falsely attributed to the first layer of one of the hosts. Nevertheless, the volume of potentially misclassified guest phase regions is small relative to the total guest phase volume. Therefore, although θ_{att} may be slightly overestimated, it provides a reliable estimate of the correct order of magnitude of the attached guest particle fraction.

For the coating process investigated in this study, an attached guest particle fraction of approximately 36 % was determined. Consequently, about 64 % of the PTFE particles are classified as unattached after the MF process. This number must be considered in relation to the distribution of the SAC of the aggregates. Despite the attainment of fully coated states, the presence of host particles with low SAC remains significant. For the same guest particle weight ratio, the process parameters could therefore first be optimized to achieve a narrower SAC distribution with the peak density in the range from 0.6 to 1.0. Subsequently, the fraction of attached guest particles can be determined once more. In further experiments, the guest particles weight ratio can be reduced by the fraction of any still uncoated guest material.